JEM Journal of Experimental Medicine

BRIEF DEFINITIVE REPORT

The XCL1–XCR1 axis supports intestinal tissue residency and antitumor immunity

Amir Ferry[1], Kianoosh M. Mempel[1], Alexander Monell[1], Miguel Reina-Campos[1,2], Nicole E. Scharping[1], Maximilian Heeg[1], Kennidy K. Takehara[1], Shiruyeh Schokrpur[3], Ning Kuo[3], Robert Saddawi-Konefka[3], J. Silvio Gutkind[3], and Ananda W. Goldrath[1,4]

Tissue-resident memory T cells (T_{RM}) provide frontline protection against pathogens and emerging malignancies. Tumor-infiltrating lymphocytes (TIL) with T_{RM} features are associated with improved clinical outcomes. However, the cellular interactions that program T_{RM} differentiation and function are not well understood. Using murine genetic models and targeted spatial transcriptomics, we found that the CD8⁺ T cell–derived chemokine XCL1 is critical for T_{RM} formation and conventional DC1 (cDC1) supported the positioning of intestinal CD8⁺ T cells during acute viral infection. In tumors, enforced *Xcl1* expression by antigen-specific CD8⁺ T cells promoted intratumoral cDC1 accumulation and T cell persistence, leading to improved overall survival. Notably, analysis of human TIL and T_{RM} revealed conserved expression of *XCL1* and *XCL2*. Thus, we have shown that the XCL1–XCR1 axis plays a non-cell autonomous role in guiding intestinal CD8⁺ T_{RM} spatial differentiation and tumor control.

Introduction

Upon antigen recognition, CD8⁺ T cells undergo proliferation and differentiate into cytotoxic effector cells capable of killing infected cells. Effector T cells are heterogeneous and include a subset that establishes a memory population, which can persist for a lifetime following antigen clearance (Chang et al., 2014). The majority of memory T cells are not found in circulation but rather lodged in tissues (Steinert et al., 2015). These tissue-resident memory T cells (T_{RM}) facilitate rapid responses via their localization in non-lymphoid tissues (NLT), providing sentinel activity during a secondary response (Schenkel et al., 2014). Cell fate specification requires the coordinated activity of multiple cell-intrinsic and environmental factors, reflective of adaptations supporting NLT trafficking, differentiation, and recall response. T_{RM} display a hybrid of memory and effector cell characteristics, retaining cytotoxicity and recall potential despite the expression of factors associated with differentiated T cell subsets (Milner and Goldrath, 2018). Studies of T_{RM} suggest that these cells may represent an ideal population for therapeutic targeting in cancer (Okła et al., 2021). Indeed, we have previously shown that modulation of T_{RM} regulatory factors can improve antitumor immunity (Milner et al., 2017; Reina-Campos et al., 2023).

Recently, single-cell RNA sequencing (scRNA-seq) has revealed similar heterogeneity within tumor-infiltrating lymphocyte (TIL) populations, reflecting a spectrum of cell states linked to tissue surveillance, memory potential, and cytotoxicity (van der Leun et al., 2020; Giles et al., 2023). Upon differentiation, CD8⁺ TIL lose self-renewal capacity and polyfunctionality until reaching exhaustion, a hypofunctional T cell state driven by chronic antigen stimulation and immunosuppressive signals (Wherry et al., 2003). Progenitor-exhausted CD8⁺ T cells (T_{PEX}) are characterized by high *Tcf7* expression and proliferate upon anti-PD1 treatment, giving rise to effector cells that eventually succumb to exhaustion (Hudson et al., 2019; Jansen et al., 2019; Miller et al., 2019; Siddiqui et al., 2019). The balance of these subsets has varying effects on the overall immune response depending on tumor type (Sade-Feldman et al., 2018; Miller et al., 2019; Escobar et al., 2023). Evidence from human patients and mouse in vivo studies suggests that differential interactions with antigen-presenting cells (APC) may regulate these states (Jansen et al., 2019; Stoltzfus et al., 2021; Wang et al., 2023). CD8⁺ TIL which resemble T_{RM} have been identified in both mouse and human studies and are consistently associated with improved prognoses (Ganesan et al., 2017; Savas et al., 2018; Park et al., 2019; Milner et al., 2020; Banchereau et al., 2021; Okła et al., 2021). While the degree of regulatory overlap between T cell exhaustion and residency is unclear, defining the signals that endow TIL with T_{RM} properties will enable the development of new immunotherapies (Schenkel and Pauken, 2023).

CD8⁺ T cell fates are conditioned by APC interactions during priming (Mempel et al., 2004). Conventional dendritic cells (DC)

[1]School of Biological Sciences, University of California, San Diego, La Jolla, CA, USA; [2]La Jolla Institute for Immunology, La Jolla, CA, USA; [3]Moores Cancer Center, University of California San Diego, La Jolla, CA, USA; [4]Allen Institute for Immunology, Seattle, WA, USA.

Correspondence to Ananda W. Goldrath: agoldrath@ucsd.edu.

are segregated into two subsets found in mice and humans, cDC1 and cDC2. cDC1 are identified via expression of *Clec9a*, *Itgae*, *Xcr1*, and *BDCA3* (human) and are key for antigen cross-presentation and pro-inflammatory cytokine production, while cDC2 promote $CD4^+$ T cell responses (Wculek et al., 2020). Recent reports have studied the role of cDC1 in shaping T cell differentiation during chronic viral infection (Dähling et al., 2022; Domenjo-Vila et al., 2023). It was demonstrated that cDC1 are critical for the maintenance of the $TCF1^{hi}$ state during anti-PD-L1 treatment. Loss of cDC1 led to a reduction of CXCR5 and CCR7 ligands, disrupting the localization of splenic T cells. It has become evident that DC subtypes modulate T cell differentiation in lymphoid and NLT, via cytokines (Iborra et al., 2016), and expression of TGFβ-activating integrins (Mani et al., 2019). In humans, $CD1c^+$ $CD163^+$ DCs preferentially induce T_{RM} features during in vitro co-culture, enabling accumulation in human epithelial grafts in mice (Bourdely et al., 2020). Whether $CD8^+$ T cells utilize chemokines to facilitate DC contacts during T_{RM} formation is not well established.

Chemokines are secreted proteins that guide the spatial organization of immune cells (Ozga et al., 2021). In human tumors, CXCL13-producing T cells associate in tertiary lymphoid structures, lymph node–like aggregates that mediate DC–T cell interactions (Sautès-Fridman et al., 2019). The IFN-γ-inducible protein CXCL10 is also produced by $CD8^+$ T cells during lymph node priming to amplify the effector response (Peperzak et al., 2013). While studies have observed differential expression of chemokines in T cell subsets during infection and cancer (Miller et al., 2019; Di Pilato et al., 2021), their contribution to the development of tissue residency is not well appreciated.

Here, we found that XCL1 promotes intestinal $CD8^+$ T_{RM} formation and TIL activity utilizing acute lymphocytic choriomeningitis virus (LCMV-Arm) and melanoma (B16), respectively. Perturbation of this axis influences the distribution and differentiation of antigen-specific $CD8^+$ T cells. Human data support modulating cDC1-$CD8^+$ T cell interactions to improve the antitumor immune response. Collectively, our study demonstrates a pivotal role for XCL1 in facilitating intestinal T_{RM} development and supports efforts to study T_{RM} factors in oncology.

Results and discussion

Elevated expression of *Xcl1* in T_{RM} and T_{PEX} cells

To identify genes relevant in T_{RM} biology, we overlayed gene lists derived from published bulk RNA-seq studies. First, we isolated genes induced in $CD8^+$ T cells by TGFβ, an established regulator of T_{RM} differentiation (Zhang and Bevan, 2013; Nath et al., 2019). Second, we included the core T_{RM} signature (Milner et al., 2017) to identify genes broadly relevant to T_{RM} cell fate. Finally, we incorporated genes of T_{PEX} $CD8^+$ T cells isolated from murine tumors (Miller et al., 2019). *Xcl1* is conserved across all three datasets (Fig. 1 A), suggesting the functional relevance of this chemokine in tissue residency and T cell differentiation.

Further analysis of T cell datasets also demonstrated high expression of *Xcl1* in the T_{PEX} population during chronic LCMV-Cl13 (Fig. S1 A). Previous assay for transposase-accessible chromatin sequencing (ATAC-seq) profiling of T_{PEX} cells demonstrated high chromatin accessibility at the *Xcl1* locus compared to exhausted T cell subsets (Jadhav et al., 2019). We also confirmed that *Xcl1* transcription was not primarily induced by tissue digestion (Fig. S1 B).

XCL1 is a chemokine produced by activated $CD8^+$ T and natural killer (NK) cells (Dorner et al., 2002), and the cognate receptor XCR1 is selectively expressed by cross-presenting cDC1 cells (Dorner et al., 2009). Mice lacking $XCR1^+$ DCs exhibit homeostatic defects in intestinal T cell populations, including $TCR\alpha\beta^+$ $CD103^+$ $CD8^+$ T cells (Ohta et al., 2016). In tumors, loss of the cDC1 transcription factor *Batf3* (Hildner et al., 2008) impairs antitumor immunity, in part due to defective DC trafficking of tumor antigen (Spranger et al., 2017). Additionally, NK cell–derived XCL1 facilitates cDC1 recruitment to the tumor microenvironment (TME), promoting antitumor immunity (Böttcher et al., 2018). However, the role of $CD8^+$ T cell–derived XCL1 during infection and tumor challenge has not been thoroughly investigated.

Analysis of P14 T cell scRNA-seq following LCMV-Arm (Kurd et al., 2020) demonstrated that *Xcl1* is highly expressed by $CD8^+$ T cells isolated from the intraepithelial layer (IEL) of the small intestine (SI) compared with circulating $CD8^+$ T cells (Fig. 1 B). Analysis of RNA-seq data profiling T_{RM} populations (Crowl et al., 2022) showed high *Xcl1* expression in all T_{RM} compared with circulating P14 T cells, with the highest levels in the SI and salivary gland (Fig. S1 C). We confirmed the high expression of *XCL1* and its paralog *XCL2* in human ileum $CD8^+$ T_{RM} (Boland et al., 2020) compared to peripheral blood mononuclear cells (PBMC) (Fig. 1 C). Human lung $CD8^+$ T_{RM} also express *XCL1*, in line with *Xcl1* being part of the core T_{RM} signature (Fig. S1 C). Thus, *Xcl1* is preferentially expressed by mouse and human $CD8^+$ T_{RM}, with elevated expression in the SI.

Given the selectivity of XCL1 for its cognate receptor XCR1 (Lei and Takahama, 2012), we asked whether SI $CD8^+$ T cells can be observed near $XCR1^+$ DC during viral infection. We adoptively transferred LCMV GP_{33-41}-specific P14 T cells into congenically distinct mice and infected them with LCMV-Arm. During the effector phase, T cells infiltrate the intestine, while cDC1 frequency decreases, likely reflecting antigen-dependent migration to lymphoid organs. At day 8 (D8), we observed P14 T cells and cDC1 in proximity in the lamina propria (LP). Following antigen clearance, P14 T cells contract and LP cDC1 frequencies return to baseline (Fig. 1 D). Interestingly, we also observed contacts between both cell types at D35 (Fig. 1 E). Given the high expression of *Xcl1* at memory time points, we hypothesized a role for this pathway in T_{RM} differentiation and sought to perturb this chemokine axis.

$CD8^+$ T cell–derived XCL1 is critical for SI T_{RM} formation

scRNA-seq of P14 T cells during LCMV-Arm (Kurd et al., 2020) demonstrates that *Xcl1* expression in the SI gradually increases and remains elevated at D90 (Fig. 2 A). We hypothesized that disrupting XCL1 production may influence memory T cell formation. Several studies have demonstrated functional interactions between $XCR1^+$ cDC1 and XCL1-producing NK cells in tumors and lymphoid tissues (Barry et al., 2018; Ghilas et al.,

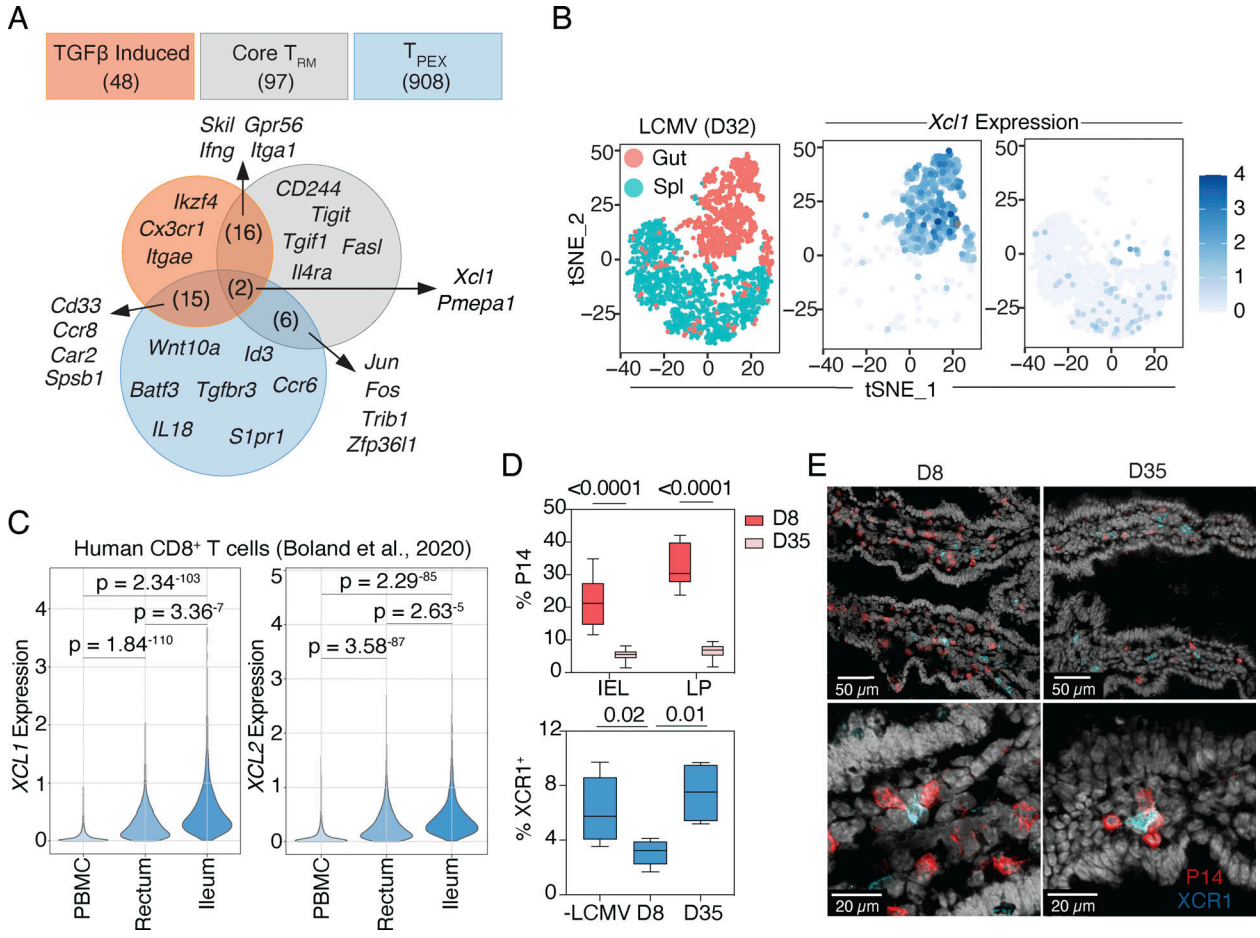

Figure 1. **XCL1 is a tissue residency–associated chemokine. (A)** Venn diagram of differentially expressed genes derived from bulk RNA-seq data (data from Milner et al. [2020]; Miller et al. [2019]; Nath et al. [2019]). **(B)** scRNA-seq displaying *Xcl1* expression in CD8⁺ isolated from spleen and IEL D32 following LCMV-Arm infection (data from Kurd et al. [2020]). **(C)** Expression of *XCL1* and *XCL2* in human CD8⁺ T cells sorted from healthy donor PBMC, rectum, and ileum (data from Boland et al. [2020]). **(D)** Quantification of P14 (IEL and LP) and XCR1⁺ DC (LP) during LCMV-Arm. **(E)** Confocal microscopy (left) of murine SI following P14 adoptive transfer and LCMV-Arm (D8 and D35 after infection). Colors are indicated, and scale bar is shown. P values shown, paired two-tailed *t* test (C), and two-way ANOVA (D). Data are pooled from at least two independent replicates, *n* = 6 per group (D and E).

2021). As an alternative to germline *Xcl1* KO mice, we leveraged the CRISPR-RNP system (Nüssing et al., 2020) to test a role for CD8⁺ T cell–derived XCL1 (Fig. S2 A). P14 T cells were electroporated with sg*Thy1* or sg*Xcl1* prior to single transfer and infection with LCMV-Arm. Tissues were harvested at effector (D8) and memory (D25) time points for analysis (Fig. 2 B).

No differences in absolute P14 T cell number or phenotype were observed in any tissues at D8 (Fig. 2 C). Recent work demonstrated that T_{RM} precursors partially upregulate the T_{RM} gene signature upon mesenteric lymph node (mLN) priming, including expression of *Ccr9*, *Xcl1*, and *P2rx7* (Qiu et al., 2023). Given the capacity of mLN and Peyer's patch–derived DCs to produce CCR9-inducing retinoic acid (RA) (Mora et al., 2003; Iwata et al., 2004; Molenaar et al., 2011), we tested whether cells exhibit differences in CCR9 during the effector phase. We observed no differences between sg*Thy1* and sg*Xcl1* cells at D8 (Fig. 2 C). Thus, *Xcl1* KO does not appear to impair effector migration into tissue. At D25, no significant differences in frequency or number were observed in the circulatory compartment (Fig. 2 D). However, we observed a marked reduction in both frequency and number of intraepithelial lymphocyte CD69⁺ CD103⁺ P14 T cells. This was accompanied by a corresponding increase in the frequency of CD69⁻ CD103⁻ cells (Fig. S2 B). No significant differences were observed in the LP or kidney (Fig. 2, E and F). P2RX7 is an extracellular ATP scavenger receptor and target of RA (Heiss et al., 2008). It has also been shown to promote TGFβ sensing and T_{RM} homeostasis (Borges da Silva et al., 2020). Control P14 T cells (*sgThy1*) express P2RX7 upon upregulation of CD69 and CD103 (Fig. 2 G), and we observed a reduced frequency and number of CD69⁺ P2RX7⁺ cells in *Xcl1* KO cells (Fig. 2 F). Loss of P2RX7 supports previous work examining defective OT-I responses in *Itgax-cre.Irf8*$^{fl/fl}$ mice following oral antigen administration (Luda et al., 2016). Together, these data demonstrate a role for T cell–derived XCL1 in the formation of SI T_{RM} during acute viral infection.

Depletion of XCR1⁺ DC impairs SI CD8⁺ T cell accumulation during LCMV-Arm

To further dissect the role of XCL1/XCR1 in cell–cell interactions influencing CD8⁺ T_{RM}, we utilized the XCR1$^{DTR/+}$ mice

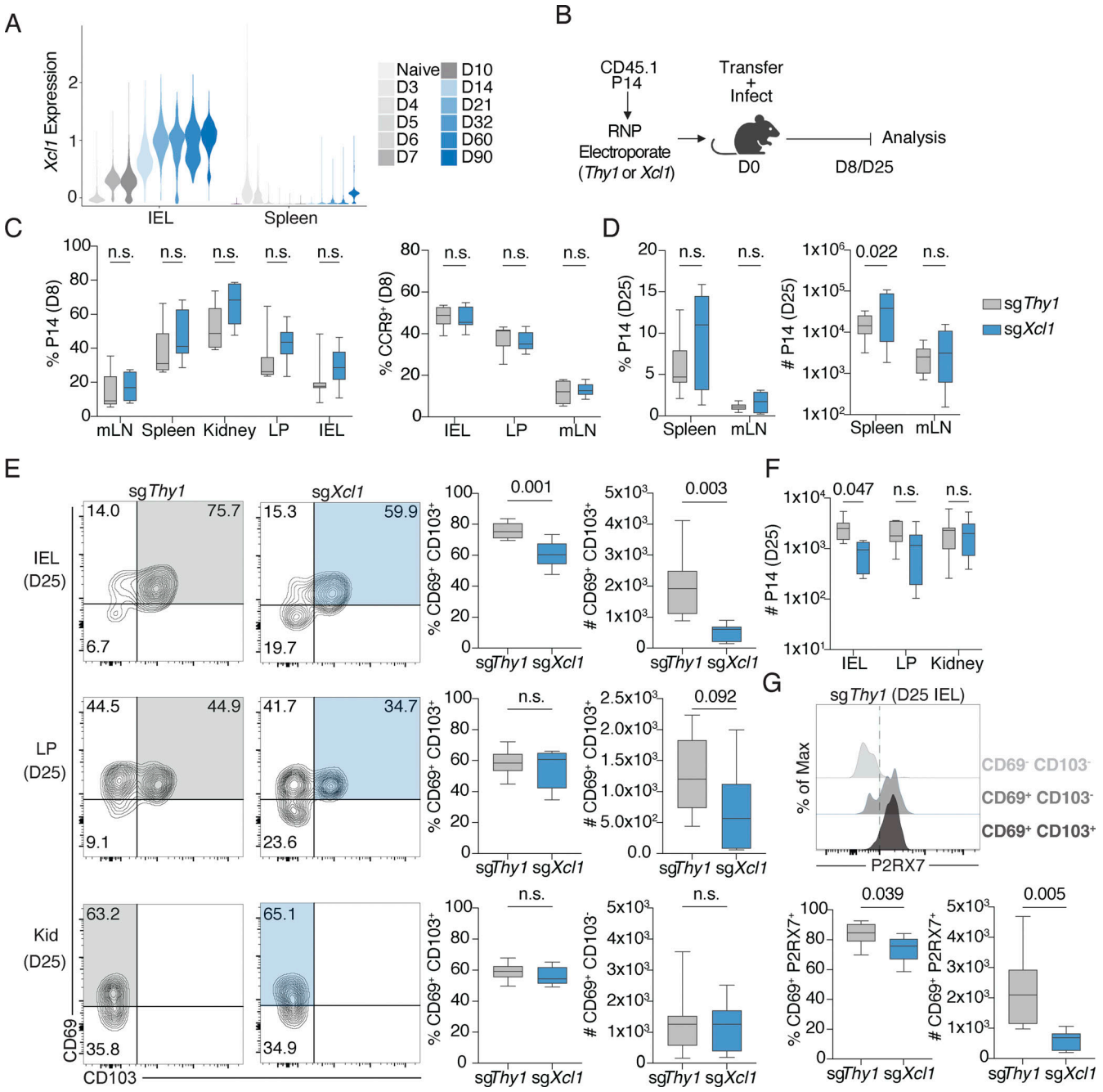

Figure 2. **Loss of *Xcl1* expression leads to defective T_{RM} formation during acute viral infection. (A)** scRNA-seq expression of *Xcl1* in P14 T cells during LCMV-Arm timecourse (data from Kurd et al. [2020]). **(B)** Experiment setup in which P14 T cells were electroporated with a control (sg*Thy1*) or experimental (sg*Xcl1*) ribonucleoprotein complex. P14 T cells were transferred into congenically distinct mice prior to LCMV-Arm infection. Tissues isolated at effector (D8) and memory (D25) time points. **(C)** Quantification of P14 frequency at D8 (left), CCR9 frequency at D8 (right). **(D)** Circulating P14 T cell frequency and number D25 after infection. **(E)** Representative plots of CD69 and CD103 in indicated tissues at D25 after infection (left). Quantification of frequency and absolute number (right). **(F)** Quantification of P14 T cell number D25 after infection. **(G)** Concatenated histogram of P2RX7 expression across *sgThy1* control P14 T cell IEL subsets at D25 (top). Quantification of frequency and number of IEL CD69$^+$ P2RX7$^+$ cells at D25 (bottom). P14 T cells gated on CD8α (IV$^-$) on all tissues except the spleen. Data are pooled from two independent experiments, n = 8 (sg*Thy1*) and n = 7 (sg*Xcl1*). P values shown, n.s. = not significant. Two-way ANOVA (C, D, and F) and unpaired t test (E and G).

(Yamazaki et al., 2013), which enable depletion of XCR1$^+$ cells with diphtheria toxin (DT). We transferred P14 T cells into WT and XCR1$^{DTR/+}$ recipients, followed by LCMV-Arm infection. Although we observed no differences in *Xcl1* KO cells at D8, we hypothesized that early depletion of XCR1$^+$ cells could influence the accumulation of SI CD8$^+$ T cells. To minimize the broad effects of DC depletion on P14 T cell expansion, we administered DT days 4–7 after infection. Tissues were isolated at D8 for flow cytometry and confocal microscopy (Fig. 3 A). We confirmed systemic depletion of XCR1$^+$ DC following DT treatment (Fig. 3, B

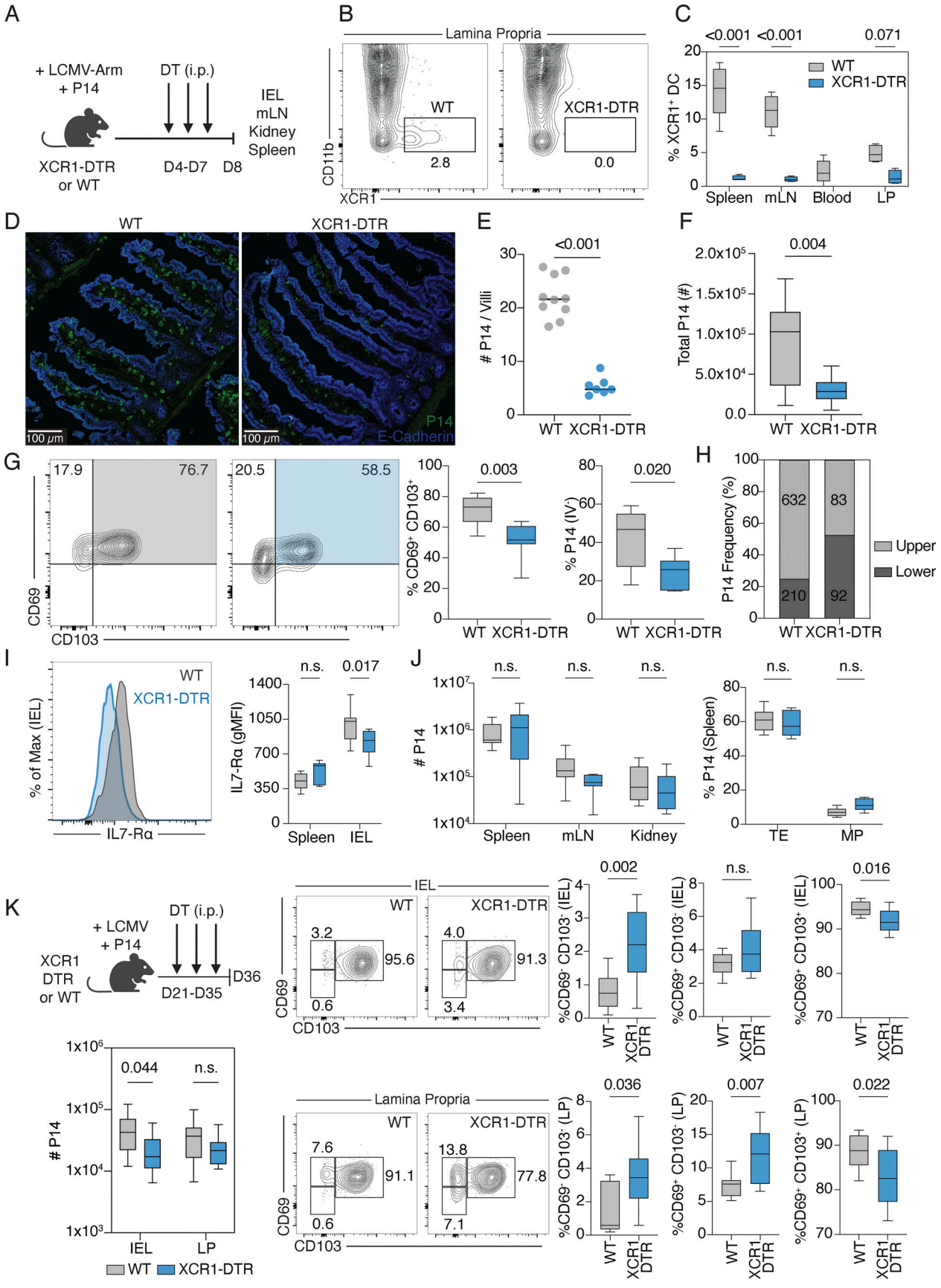

Figure 3. **XCR1⁺ DC are critical for the accumulation of SI CD8⁺ effector cells. (A)** Experiment setup in which naïve P14 cells were transferred into congenically distinct recipients (WT or XCR1-DTR) prior to LCMV-Arm infection. Both groups were treated with DT from D4–D7 of infection and sacrificed on

D8 for analysis. **(B)** Representative flow cytometry staining of DT-mediated XCR1$^+$ cell depletion (LP) pregated on CD45$^+$ MHCII$^+$ CD11c$^+$. **(C)** Quantification of XCR1$^+$ cDC1 frequency. **(D)** Representative confocal microscopy of murine SI D8 after infection. Stain is indicated in the panel. **(E)** Quantification of P14 absolute number per villi. Data are representative of two independent experiments. **(F)** Quantificaton of absolute number of IEL P14 T cells. **(G)** Representative plot of CD69 and CD103 expression in IEL P14 T cells (left) and frequency quantification (right). **(H)** Quantification of P14 T cell location across crypt-villi axis. The numbers shown indicate cell counts. **(I)** Representative histogram of CD127 gMFI (left) and quantification (right) of gMFI in spleen and IEL P14 T cells. **(J)** Absolute number of P14 T cells isolated from spleen, mLN, and kidney (left) and quantification of TE (KLRG1$^+$ CD127$^-$) and MP (KLRG1$^-$ CD127$^+$) populations (right). **(K)** Experiment setup in which naïve P14 T cells are transferred into recipients (WT or XCR1-DTR) prior to LCMV-Arm infection. Both groups were treated with DT (every 3 days) from D21–D35 of infection and sacrificed on D36 (left). Quantification of P14 T cell number (bottom) and subset frequency (right). P14 T cells gated on CD8α (IV$^-$) on all tissue except the spleen. P values are shown. Data are pooled from at least two independent experiments, (A) n = 8 (WT) and n = 7 (XCR1-DTR), (K) n = 15 (WT), and n = 15 (XCR1-DTR). Two-way ANOVA (C and I–K) and unpaired t test (E–G and K).

and C). Confocal imaging of the SI (Fig. 3 D) revealed a profound defect in P14 T cell accumulation, with an approximately threefold decrease in the number of P14 T cells (Fig. 3, E and F). Flow cytometric analysis showed a reduced frequency of CD69$^+$ CD103$^+$ cells (Fig. 3 G), suggesting impaired differentiation of T cells in the absence of cDC1. Analysis of P14 T cell location revealed a twofold increase in P14 occupying the lower half of the villus (Fig. 3 H). Additionally, IEL but not splenic P14 T cells displayed reduced expression of the IL-7 receptor alpha chain, CD127 (Fig. 3 I). Absolute numbers of P14 T cells did not differ in lymphoid tissues or the kidney, suggesting a preferential role for XCR1$^+$ DCs in intestinal immunity, in line with work studying this population during homeostasis (Ohta et al., 2016). Circulating cells revealed no differences in the proportions of terminal-effector or memory-precursor P14 T cells (Fig. 3 J).

Depletion of cDC1 following memory formation led to a frequency reduction in CD103$^+$ T_{RM} in IEL and LP compartments (Fig. 3 K). We tested a functional role for the XCR1 receptor by transferring P14 into XCR1-deficient mice (XCR1$^{Ven/Ven}$). At a memory time point, we observed a modest loss of CD103$^+$ T cells in the LP of XCR1$^{Ven/Ven}$ hosts, consistent with the maintained in situ presence of XCR1-deficient cDC1 (Fig. S2 C). Together, these data support a role for XCR1 and the cDC1 population in T_{RM} formation and maintenance, respectively.

Spatial transcriptomics profiling of WT and XCR1$^+$ cell–depleted SI

SI CD8$^+$ T cell phenotype is linked to intratissue location (Reina-Campos et al., 2024, *Preprint*). To interrogate the impact of XCR1$^+$ cell depletion on the transcriptome and location of P14 T cells, we utilized the 10X Xenium platform to measure RNA transcripts at subcellular resolution. This enables the detection of 350 genes, curated to enable high-quality cell-type annotation, ligand-receptor activities, and immune cell states.

To identify P14 T cells, we transferred *Xist*$^+$ CD45.1 female cells into male CD45.2 recipients prior to DT treatment (Fig. 4 A). We validated our previous findings that depletion of XCR1$^+$ cDC1 (Fig. S2 D) leads to a frequency reduction of CD103$^+$ P14 cells (Fig. S2 E). The loss of CD103$^+$ cells aligns with the observation that CD8$^+$ T_{RM} *Itgae* transcripts are more abundant at the villus tip (Reina-Campos et al., 2024, *Preprint*). Quantification of P14 T cells using *Xist* transcripts confirms the reduction in XCR1-DTR mice (Fig. 4 B). We generated Immune Allocation Plots (IMAP) (Reina-Campos et al., 2024, *Preprint*) to depict the localization and density along two axes: epithelial and crypt-villi (Fig. 4 C). Upon cDC1 depletion, P14 T cells mislocalized toward the base of the crypt (Fig. 4 D). Transcript images showed proximity of *Xcl1*$^+$ and *Xcr1*$^+$ cells in WT mice with comparable *Xcl1* transcript localization in WT and XCR1-DTR mice (Fig. 4 E). In mice, *Xcl1* expression increases toward the villi tip, mirroring *Itgae* and opposing *Tcf7*. In parallel, human CD8αβ$^+$ T cell *XCL1*/XCL2 displayed a similar crypt-villi expression pattern (Fig. 4 F) (Reina-Campos et al., 2024, *Preprint*). Consistent with previous studies (Kurd et al., 2020; Milner et al., 2020), the detection of P14 *Xcl1* expression increased during LCMV-Arm (Fig. S2 F). Differential gene expression of P14 T cells in WT and XCR1$^+$ cell-depleted mice revealed numerous changes (Fig. 4 G), several of which have been linked to T_{RM} development and function. This includes *Gzma* (Crowl et al., 2022), *Srebf2* (Reina-Campos et al., 2023), and *Fabp2* (Frizzell et al., 2020). P14 in XCR1-DTR mice also displayed marginally lower *Cxcr3* expression, potentially altering CXCL9/10-mediated chemotaxis (Fig. S2 G). In WT mice, proximity to cDC1 influences the expression of memory-associated genes, including *Tcf7*, *Il15ra*, *Tgfbr2*, and *Ccr9* (Fig. 4 H). Thus, disrupting CD8-cDC1 crosstalk leads to impaired localization and disrupts T_{RM}-associated gene expression.

Xcl1 overexpression enhances antitumor immunity and is a conserved feature of human T_{RM}-like TIL

T cells which share features of T_{RM} cells have been associated with positive prognoses, immunotherapy responsiveness, and CAR-T performance across multiple tumor types (Savas et al., 2018; Ganesan et al., 2017; Edwards et al., 2018; Oliveira et al., 2023; Jung et al., 2023). In parallel, studies have demonstrated the role of TCF1^{hi} T_{PEX} and cDC1 cells, particularly in response to checkpoint blockade (Im et al., 2016; Salmon et al., 2016; Miller et al., 2019; Siddiqui et al., 2019; Teijeira et al., 2022; Meiser et al., 2023).

Here, we employed an adoptive transfer model of P14 T cells into tumor-bearing mice (Fig. S3 A). P14 T cells profiled D7 after transfer consist of three differentiation states. T_{PEX} cells are marked by high expression of TCF1 and SLAMF6, while T_{INT} and T_{TERM} downregulate these markers and upregulate PD1, CD39, and Granzyme B (Fig. S3, B and C). During an endogenous response to B16 melanoma, we observed a correlated decay of intratumoral T_{PEX} and cDC1 frequencies, while these populations remained stable in the tumor-draining lymph node. Given the high expression of *Xcl1* by T_{PEX} (Fig. 5 A), we hypothesized that enhancing XCL1 production could rescue cDC1 abundance and modulate differentiation. We transduced P14 T cells with an *Xcl1* overexpression (CD8^{Xcl1}) or empty vector construct (CD8^{EV}) (Fig. S3 D) and transferred cells into tumor-bearing mice. At D4–6

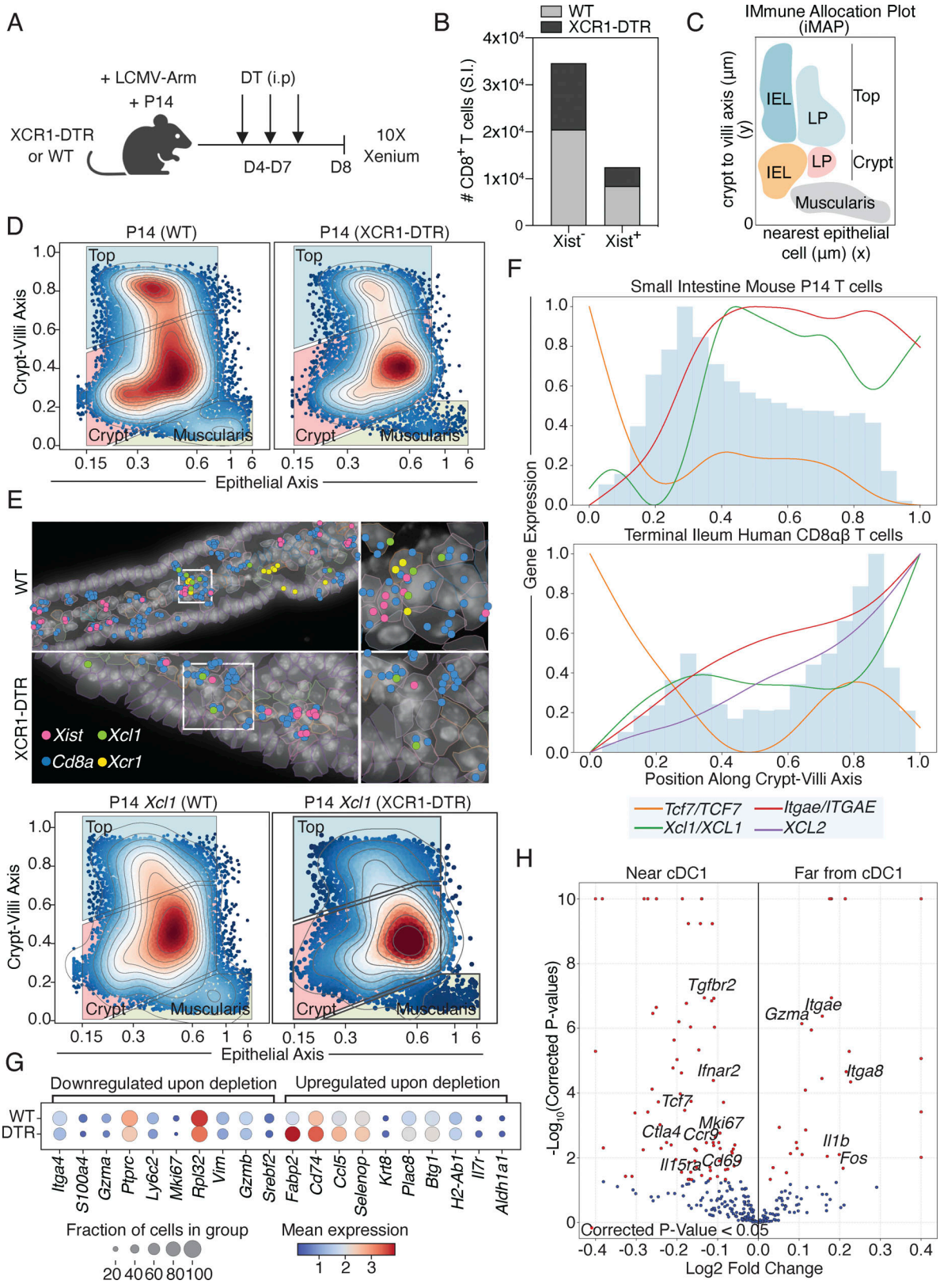

Figure 4. **Spatial transcriptomics profiling of WT and XCR1⁺ depleted mice during LCMV-Arm. (A)** Experimental schematic in which naïve female P14 T cells (Xist⁺) were transferred into male B6 mice followed by LCMV-Arm infection. DT administered D4–D7 after infection prior to tissue isolation at D8. **(B)** Quantification of CD8⁺ T cell absolute number (Xist⁻ and Xist⁺) in whole tissue section. **(C)** IMAP schematic of SI villus. **(D)** IMAP plots of P14 T cell distribution and density in WT and XCR1⁺ cell–depleted mice. **(E)** Representative image of transcript detection in WT and XCR1-DTR SI; colored dots correspond to labeled genes (top). Representative IMAP plots displaying P14 *Xcl1* in WT and XCR1-DTR mice (bottom). **(F)** Histogram of gene expression in mouse (SI P14) and human

(CD8αβ) T cells along crypt-villi axis. Gene labels shown, shaded bars represent T cell density. **(G)** Heatmap of differential gene expression in P14 T cells from WT and XCR1$^+$ cell depleted mice. **(H)** Volcano plot displaying differential gene expression relative to P14 T cell proximity to XCR1$^+$ cDC1 cells. $-Log_{10}$(Corrected P values) displayed. Flow validation (n = 3 per group) is representative of three independent replicates and spatial transcriptomics (n = 1 per group).

after transfer, we observed a tumor-specific accumulation of XCR1$^+$ DC in mice receiving CD8^{Xcl1} (Fig. 5 B). At D6 after transfer, CD8^{Xcl1} mice had a higher frequency of intratumoral P14 T cells. TIL analysis revealed a significant increase in TCF1 and KI67, reflecting enhanced persistence and proliferation (Fig. 5 C). Transfer of CD8^{Xcl1} led to delayed tumor growth and prolonged survival during B16-GP$_{33–41}$ melanoma challenge. Similar results were also observed using the MC38-GP$_{33–41}$ colorectal carcinoma model (Fig. 5 D and Fig. S3 E).

XCL1 has not been extensively studied in human T cells. Analysis of a T cell atlas (Zheng et al., 2021) provides single-cell expression data across 21 tumor types. Cluster analysis shows an enriched expression of *XCL1* and *XCL2* in four populations: NK-like (Tk.*KIR2DL4*, Tk.*TYROBP*), *TCF7*^{hi} (Tex.*TCF7*), and T$_{RM}$-like (Trm.*ZNF683*) (Fig. 5 E and Fig. S3 F), matching the murine expression patterns. Further, analysis of TCGA data of 457 skin cutaneous melanoma (SKCM) patients demonstrates survival stratification based on *XCL1/XCL2* expression. *XCL1/XCL2* also correlated with a functional cDC1 signature (Meiser et al., 2023) (Fig. 5 F). The top 20 genes with similar expression pattern as *XCL1* include immune activation and T$_{RM}$ genes, such as *GZMA*, *TIGIT*, *CCL4*, and *CXCR6* (Hombrink et al., 2016; Kumar et al., 2017) (Fig. S3 G). Thus, the human expression profile supports exploration of the XCL1–XCR1 axis, for example as a target for TME remodeling from "cold" to "hot" prior to immunotherapy initiation.

In summary, we demonstrate that CD8$^+$ T$_{RM}$ highly express the cDC1 chemoattractant, *Xcl1*. Intestinal CD8$^+$ T cells upregulate *Xcl1* during infection and expression remains elevated following clearance. Depletion of cDC1 impaired the localization and differentiation of SI CD8$^+$ T cells during LCMV-Arm. Further, T cell–specific KO of *Xcl1* leads to defective T$_{RM}$ formation. The selective expression of TGFβ activating integrin *Itgb8* and RA enzyme *Aldh1a2* in XCR1$^+$ DCs (Shiokawa et al., 2017) supports a role for these cells in T$_{RM}$ differentiation. Additionally, the expression of *Tgfb1* in LP cDC1 suggests a role in maintaining T cell *Itgae* expression (Reina-Campos et al., 2024, *Preprint*). While the bidirectional signal exchange between cDC1 and CD8$^+$ T cells remains to be investigated, our data suggest a role for interactions at effector and memory time points. In tumors, the proinflammatory functions of cDC1, such as IL-12 production, may favorably remodel the TME to support T cell infiltration and survival. Further studies are needed to understand the regulation of intratumoral niches, given their presence in human cancers (Jansen et al., 2019; Wang et al., 2023).

These findings highlight the importance of studying cell–cell interactions which shape tissue immunity (Nakandakari-Higa et al., 2024). These efforts will be strengthened by advances in spatial transcriptomics, enabling high-resolution exploration of cellular states in healthy and diseased tissues. Defining regulators of *Xcl1* (Lei et al., 2011; Russ et al., 2014) and *Xcr1* (Bayerl et al., 2023), particularly across tissue environments will inform strategies to harness the T$_{RM}$ interactome for solid tumor immunotherapy.

Materials and methods

Mice

All mice were bred on the C57BL6/J background and housed in specific pathogen–free conditions in accordance with the Institutional Animal Care and Use Committees (IACUC) of the University of California, San Diego (UCSD). Both male and female mice were used throughout the study, with sex-matched T cell donors and recipients (or female donor cells transferred into male recipients) and between 1.5- and 4-mo-old. C57BL/6J mice (stock #000664; The Jackson Laboratory), XCR1$^{DTR/Venus}$ (Gutkind Laboratory, UCSD), P14 mice (with transgenic expression of H-2D^b-restricted TCR specific for LCMV glycoprotein GP 33–41; stock #037394-JAX; The Jackson Laboratory), CD45.1$^+$ and CD45.1.2$^+$ congenic mice were bred in house.

T cell activation, transduction

For P14 CD8$^+$ T cell activation, naive CD8$^+$ T cells from spleens and lymph nodes were negatively enriched with LS MACS columns (Miltenyi Biotec) using biotin anti-CD4 (GK1.5), anti-Ter119 (TER-119), anti-GR-1 (RB6-8C5), anti-MHCII (M5/114.15.2), anti B220 (RA3-6B2), and anti-NK 1.1 (PK136). P14 cells (2 × 10^6) were plated in a well of a 6-well plate that was precoated with 100 µg/ml goat anti-hamster IgG (H+L; Thermo Fisher Scientific). The activation medium contained 1 µg/ml anti-CD3 (145-2C11) and 1 µg/ml anti-CD28 (37.51) (eBioscience). Culture medium was replaced after 18 h of activation with retroviral supernatant mixed with 50 µM BME and 8 µg/ml polybrene (Millipore) followed by spin-infection (1-h centrifugation at 2,000 RPM, 37°C). The plate was incubated at 37°C for 3 h after spin-infection, and then the retroviral supernatant was replaced by T cell medium supplemented with IL-2 (Peprotech) and incubated for 24–72 h prior to use.

Retroviral production

For enforced *Xcl1* expression, retroviral particles were generated using platinum E cells grown in 10-cm plates with full selection media (DMEM, 10% FBS [vol/vol], 2 mM L-glutamine, 100 U/ml penicillin-streptomycin, 1 µg/ml puromycin, and 10 µg/ml blasticidin). 18 h before transfection selection media was replaced with antibiotic-free media (DMEM, 10% FBS, 2 mM L-glutamine). For each 10-cm plate, 10 µg of each construct and 5 µg of pCL-Eco helper plasmids were mixed in Opti-MEM (Thermo Fisher Scientific) to a volume of 700 µl. This was combined with 45 µl of TransIT-LT1 reagent (Mirus Bio) and 655 µl of Opti-MEM for 20 min at room temperature. This mixture was added dropwise to each 10-cm plate. 12 h later media was replaced, and the viral supernatant was subsequently harvested at 48 and 72 h.

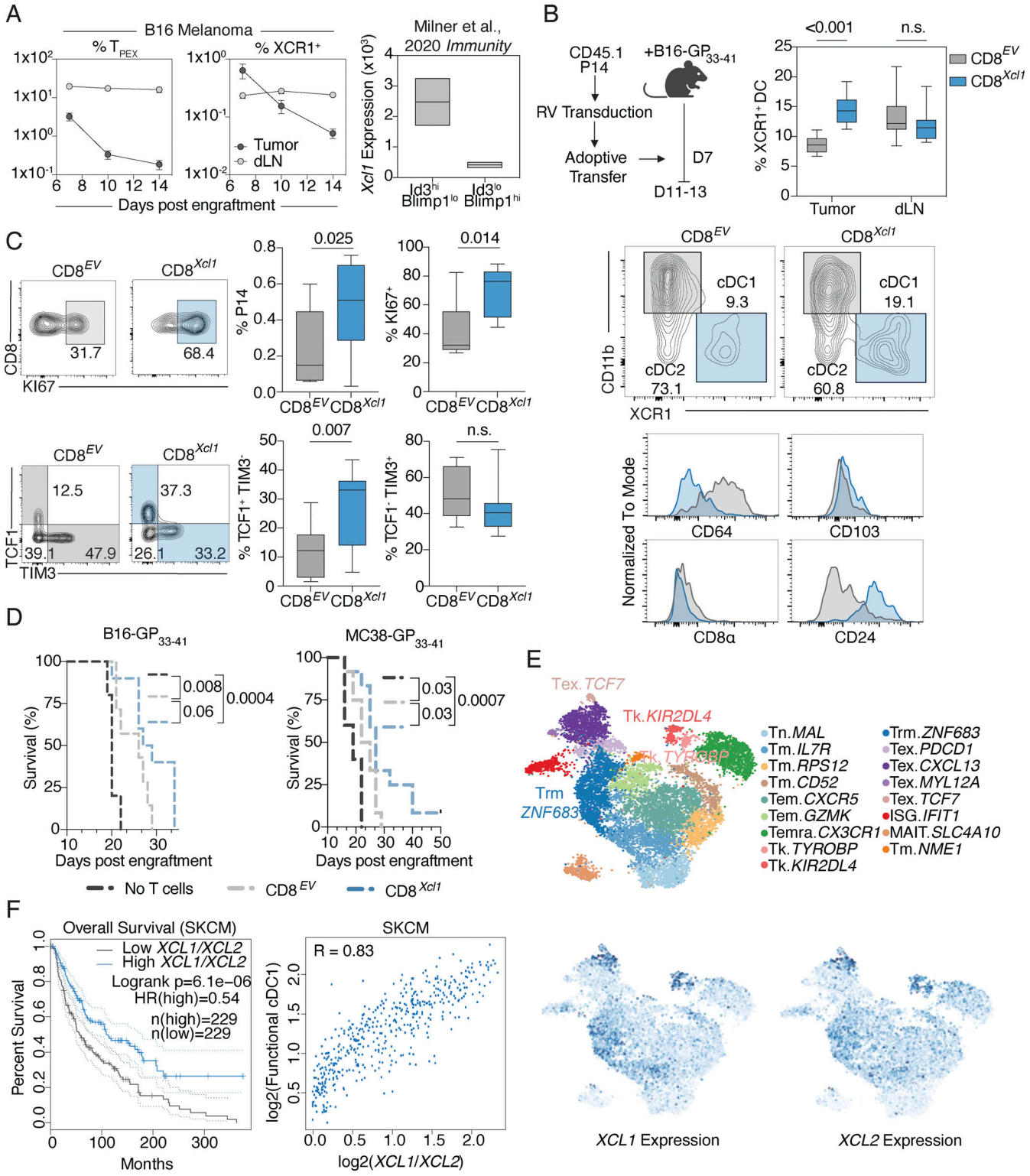

Figure 5. **Overexpression of *Xcl1* in CD8⁺ T cells enhances antitumor immunity. (A)** Frequency plots of indicated endogenous cell type following B16 inoculation (left) and RNA expression of *Xcl1* in Id3^{hi} and Id3^{lo} subsets from Milner et al. (2020). *n* = 4 per time point. **(B)** Experimental schematic where congenically distinct P14 T cells were transduced with empty vector (CD8^{EV}) or *Xcl1* (CD8^{Xcl1}) encoding retrovirus and transferred into tumor-bearing mice (B16-GP$_{33-41}$) (left) and frequency of XCR1⁺ cDC1 in indicated tissue (right), *n* = 8 (CD8^{EV}) and *n* = 12 (CD8^{Xcl1}). **(C)** Representative flow cytometry plots of KI67, TCF1, and TIM3 in intratumoral P14 T cells and corresponding quantification, *n* = 10 (CD8^{EV}) and *n* = 13 (CD8^{Xcl1}). **(D)** Kaplan-Meier curve of mouse survival in indicated tumor type with log-rank (Mantel-Cox) test. Tumor area was monitored every 2–3 days, *n* = 5 (no T cells), *n* = 10 (CD8^{EV}), and *n* = 13 (CD8^{Xcl1}). **(E)** scRNA-seq clusters (top) derived from pan-cancer atlas (Zheng et al., 2021), subset labels shown. *XCL1* and *XCL2* expression (bottom) within cluster UMAP. **(F)** TCGA melanoma (SKCM) patient survival curve (left) based on *XCL1*/*XCL2* expression and correlation with functional cDC1 signature (Meiser et al., 2023). Data representative (B, C, G, and H) or pooled (D–F) from at least two independent studies. P values shown. Two-way ANOVA (B), unpaired *t* test (C), log-rank Mantel-Cox test (D).

Cell culture

Male B16 melanoma cells and MC38 colorectal tumor cells expressing the LCMV glycoprotein epitope amino acid 33–41 (B16-$GP_{33–41}$) and female PLAT-E cells were maintained in DMEM containing 5% bovine growth serum, 1% HEPES, and 0.1% 2-mercaptoethanol. Both cell lines have been confirmed to be free of mycoplasma through quantitative PCR (qPCR).

Tumor studies

B16-$GP_{33–41}$ cells and MC38-$GP_{33–41}$ (5×10^5) were transplanted subcutaneously into the right flank of wild-type mice. After tumors became palpable, 7–9 days after transplantation, 1–2.5 × 10^6 P14 cells transduced with *Xcl1* or *EV* retroviral constructs and expanded in vitro with 50 U/ml IL-2 (Peprotech) for 2–3 days were transferred intravenously. Tumors were monitored daily and mice with ulcerated tumors or tumors exceeding 1,500 mm^3 in size were euthanized in accordance with UCSD IACUC. TIL were isolated as previously described (Milner et al., 2017) 4–8 days following adoptive transfer.

Infection studies

Mice were infected with 2×10^5 pfu lymphocytic choriomeningitis virus-Armstrong (LCMV) by intraperitoneal injection. For naive P14 transfers, 5×10^4 congenically distinct cells per recipient mouse were adoptively transferred prior to infection. To distinguish vascular-associated $CD8^+$ T cells in certain NLT (salivary gland, kidney, IEL, and mLN), 3 µg of CD8α conjugated to APC eFlour780 was injected i.v. into mice 3 min prior to sacrifice and organ excision. Cells lacking CD8α labeling were considered localized within NLT.

RNA-seq data

Bioinformatic analyses of RNA-seq data derived from the following studies: GSE122713, PRJNA497086, GSE149879, GSE182276, GSE94964, GSE125527, GSE147502, GSE131847, GSE156728, GSE107395, GSE125471. Spatial transcriptomics (WT and XCR1-DTR) GSE accession: GSE280895 and GSE284741.

CRISPR Cas9 targeting

1 day after activation, T cells were electroporated with complexed tracrRNA (IDT), Cas9 (UC Berkeley), and crRNA (IDT). crRNA targeting Thy1 (control) was used alone as a control and was mixed with the conditional crRNA to be used as a marker of electroporated cells (Nüssing et al., 2020). Electroporated cells were cultured in 50 U/ml of IL-2 for 24–48 h. Control and experimental cells (500K/mouse) were transferred into congenically distinct recipients prior to LCMV infection. DNA modifications were quantified using TIDE (Brinkman et al., 2018) and gene expression changes by qPCR. The sgRNA sequence for *Xcl1* targeting is the following: 5′-AGUCUGCUGCCUCACCCCAU-3′. The sgRNA sequence for *Thy1* targeting is the following: 5′-CCGCCAUGAGAAUAA CACCAGUUUUAGAGCUAUGCU-3′.

RT-qPCR

50,000 cells were sorted directly into Trizol, and RNA was extracted by chloroform and isopropanol precipitation. cDNA was synthesized using Superscript IV (Life Technologies) following the manufacturer's instructions and qPCR was performed using the Stratagene Brilliant II Syber Green master mix (Agilent Technologies). RT-PCR *Xcl1* (F) 5′-CTTTCCTGGGAGTCTGCTGC-3′ Xcl1 (R) 5′-CAGCCGCTGGGTTTGTAAGT-3′, Hprt1 (F) 5′-TGA AGAGCTACTGTAATGATCAGTCAAC-3′, *Hprt1* (R) 5′-AGCAAG CTTGCAACCTTAACCA-3′.

Immunohistochemistry

Mice were sacrificed by CO_2 asphyxiation. Following removal of the SI, duodenums were resected, cut open longitudinally, washed with ice-cold PBS, and shaped into a swiss roll before OCT embedding (Sakura). Samples were snap-frozen on dry ice and stored at −80°C until sectioning. 10 µm cryo-sections were prepared on Superfrost plus glass slides (Fisher Scientific) using the CryoStar NX50 cryostat (Thermo Fisher Scientific) at a cutting temperature of −19°C. Following sectioning, slides were gently washed once in prechilled 1× PBS (Gibco) for 3 min, then fixed immediately in prechilled acetone at −20°C for 20 min. Next, slides were washed for 3 min with 1× PBS to remove residual acetone and blocked using Dako Protein Block (Agilent) for 3 h at RT in the dark. After blocking, primary conjugated antibodies were diluted in Dako antibody diluent with background reducing components (Agilent) at 1:50. Antibodies included CD8a (53-6.7), CD45.1 (A20), CD324 (DECMA-1), XCR1 (ZET), and CD11c (N418). Slides were left to stain overnight at 4°C in a dark humidified chamber. Afterward, slides were moved to RT and left for 1 additional hour to increase staining signal on weakly expressed epitopes. Slides were washed 2× for 10 min with 1× PBS-T (0.1% Triton X-100 [Sigma-Aldrich]) and 2× for 10 min with 1× PBS with gentle agitation. Following the washing step, a nuclear counterstain (DAPI; BioLegend) was added at 1:1,000 diluted in 1× PBS for 5 min at RT in the dark. To remove excess counterstain, slides were washed one last time (5 min in 1× PBS) and air-dried for 1 min in the dark before being mounted in Vectashield Vibrance Mounting Medium (Vector Laboratories). Slides were left to cure for 1 h at room temperature in the dark before imaging on a Zeiss LSM700 confocal microscope using the PlanApo 20×/0.8 objective. Quantification of the average distance of P14 cells in small intestinal villi was done in ImageJ. P14 T cells located in villi were manually counted. To account for phenotypic differences in villi length, P14 T cell distance measurements were normalized and displayed as a percentage of villi distance.

DT treatment

For DT-mediated ablation of XCR1-expressing cells, 500 ng/mouse was administered by intraperitoneal injection for four consecutive days. Both WT and XCR1-DTR mice received DT treatment. For longer-term depletion, mice received 500 ng every 3 days for the course of treatment.

Preparation of single-cell suspensions

Single-cell suspensions were prepared from the spleen or lymph node by mechanical disruption. For SI preparations, Peyer's patches were excised, luminal contents were removed, and tissue was cut longitudinally then into 1 cm pieces. The SI pieces

were incubated while shaking in 10% HBSS/HEPES bicarbonate solution containing 15.4 mg/100 µl of dithioerthritol (EMD Millipore) at 37°C for 30 min to extract SIIEL. For LP lymphocyte isolation, SI pieces were further treated with 100 U/ml type I collagenase (Worthington Biochemical) in RPMI-1640 containing 5% bovine growth serum, 2 mM $MgCl_2$, and 2 mM $CaCl_2$ at 37°C for 30 min. The salivary gland, kidney, and tumor were cut with scissors into fine pieces and then incubated while shaking with 100 U/ml type I collagenase as above. Lymphocytes from all tissue but spleen and lymph node were purified on a 44%/67% Percoll density gradient.

Spatial transcriptomics analysis using 10X Xenium

Formalin fixed parrafin embedded (FFPE) tissues were sectioned to a thickness of 5 µm onto a Xenium slide, followed by deparaffinization and permeabilization following the 10X user guides CG000578 and CG000580. Probe hybridization, ligation, and amplification were done following the 10X user guide CG000582. In short, probe hybridization occurred at 50°C overnight with a probe concentration of 10 nM using a custom gene panel designed to detect 350 different mRNAs. After stringency washing to remove unhybridized probes, probes were ligated at 37°C for 2 h. During this step, a rolling circle amplification primer was also annealed. The circularized probes were then enzymatically amplified (2 h at 37°C), generating multiple copies of the gene-specific barcode for each RNA binding event. After washing, background fluorescence was quenched chemically. Sections were placed into an imaging cassette to be loaded onto the Xenium Analyzer instrument following the 10X user guide CG000584.

Spatial data processing

For 10X Xenium spatial transcriptomics data, nuclei were segmented using a fine-tuned Cellpose model on max-projected DAPI staining images. Baysor was used to predict cell boundary segmentations using the Cellpose nuclei segmentations as a prior segmentation for 10X Xenium and transcripts as input, with parameters prior-segmentation-confidence = 0.95 and 0.9, respectively, and min-molecules-per cell set to the median nucleus transcript count (see https://github.com/Goldrathlab/Spatial-TRMpaper). Baysor segmentations containing no nuclei were filtered out, and segmentations containing multiple nuclei were split by assigning transcripts to the nearest nucleus centroid within the segmentation boundary. All cells with $n < 8$ nuclear transcripts, $n < 20$ total transcripts, or $n > 800$ total transcripts were filtered out before downstream processing. To integrate spatial replicates into a joint embedding, scVI was used with *n*_layers = 2, and *n*_latent = 30. The joint embedding was projected into 2D space using scVI.model.utils.mde. Leiden clustering was performed on the scVI learned embeddings using scanpy.tl.leiden with resolution = 1, and every Leiden cluster was further subclustered at resolution = 1.2. Celltypist and GeneFormer were used for a first-pass cell type assignment, with further manual refinement based on the expression of cell type marker genes to define cell types in a Class > Type > Subtype hierarchy. Anndata format was used for all further processing.

Gene panel design for probe-based spatial transcriptomics profiling of mouse SI

For the Xenium mouse 350 gene panel, 79 SI canonical cell type marker genes were compiled from existing literature, and Xist, a marker for transferred female P14 T cells. An additional 158 genes from a Nichenet database of ligand–receptor pairs were included. Next, a supervised PERSIST was run on an immune-enriched intestine scRNA-seq dataset with the previously compiled set of genes as prior information, adding an additional 70 genes. Lastly, a supervised PERSIST was run on a SI scRNA-seq dataset to capture 59 cell-type marker genes for 350 total targets. To create the Xenium human 422 gene panel, we created a base set of canonical immune marker genes, ligand–receptor pairs, spatially differentially expressed genes within mouse P14 T cells, and IEL the 10X Genomics base human colon panel totaling 343 genes. Using this set as prior information to PERSIST, and a reference human immune cell scRNA-seq dataset, unsupervised PERSIST filled in the remaining 79 genes.

Generation of IMAPs and transcriptional IMAPs

The epithelial IMAP axis values are computed through a biexponential transformation applied to the clipped epithelial axis values across all cells. Each cell is positioned on the IMAP by its corresponding crypt–villus axis and transformed epithelial axis values. Density within the scattered point cloud is visualized using color-mapped scipy.stats.gaussian_kde values, with density lines overlaid using seaborn.kdeplot for enhanced clarity and interpretation. Gate boundaries were manually drawn to distinguish the muscularis, villus crypt, and villus top by observing the IMAP locations of cell types known to localize to each region. Transcriptional IMAPs were colored by adding an array of gene expression counts as a point weight parameter to the scipy.stats.gaussian_kde function.

Flow cytometry and cell sorting

Cells were incubated for 30 min at 4°C in PBS supplemented with 2% bovine growth serum and 0.1% sodium azide. Surface antibodies used include CD45.1 (A20), CD45.2 (104), KLRG1 (2F1), CD8a (53-6.7), CD127 (A7R34), CD62L (MEL-14), CD69 (H1.2F3), CD103 (2E7), CD90.2 (53-2.1), P2RX7 (1F11), MHCII (M5/114.15.2), CD11c (N418), CD11b (M1/70), and XCR1 (ZET). Intracellular staining of Tcf1 (C63D9), GzB (MHGB05), and Ki67 (11F6) was performed using the Foxp3/Transcription Factor Staining Kit according to the manufacturer's protocol (Tonbo). BD Cytofix/Cytoperm Solution Kit (BD Biosciences). Stained cells were analyzed using LSRFortessa or LSRFortessa X-20 cytometers (BD) and FlowJo software (TreeStar). All sorting was performed on BD FACSAria or BD FACSAria Fusion instruments.

Statistical analyses and software

Statistical parameters are reported in the figures and figure legends. A two-tailed Student's *t* test (unpaired for single transfer studies) or one-way ANOVA for studies with more than two groups was done on all reported data using Prism software (GraphPad). For survival data, a log-rank Mantel-Cox test was performed. All experiments were executed independently at

least two times to ensure reproducibility. All P values are shown in the figures. Human TCGA data were analyzed using the GEPIA 2.0 software tool (Tang et al., 2019).

Online supplemental material

Fig. S1 shows *Xcl1* RNA-seq expression in CD8$^+$ T cell subsets across published datasets. Fig. S2 shows CRISPR KO efficiency, experiments using XCR1$^{Ven/Ven}$ mice, confocal microscopy validation of XCR1$^+$ cell depletion, and additional data from the spatial transcriptomics experiment. Fig. S3 shows the experimental setup for TIL analysis, flow cytometry data, *Xcl1* overexpression validation, tumor growth curves, and human TIL scRNA-seq analysis.

Data availability

The data are available from the corresponding author upon reasonable request.

Acknowledgments

We thank the Goldrath and Gutkind laboratories for advice and manuscript review. We thank Dr. John Chang for a critical reading of the manuscript.

This work was supported by National Institutes of Health grants R01AI179952 (A.W. Goldrath), R37AI067545 (A.W. Goldrath), R01AI072117 (A.W. Goldrath), and R01AI150282 (A.W. Goldrath).

Author contributions: A. Ferry: Conceptualization, Data curation, Formal analysis, Investigation, Methodology, Validation, Visualization, Writing - original draft, Writing - review & editing, K.M. Mempel: Formal analysis, Investigation, A. Monell: Data curation, Formal analysis, Software, Visualization, M. Reina-Campos: Conceptualization, Formal analysis, Investigation, Methodology, Resources, Supervision, Writing - review & editing, N.E. Scharping: Investigation, Methodology, M. Heeg: Data curation, Formal analysis, Investigation, Methodology, Software, K.K. Takehara: Investigation, S. Schokrpur: Investigation, Methodology, N. Kuo: Resources, Validation, R. Saddawi-Konefka: Investigation, Methodology, J.S. Gutkind: Conceptualization, Investigation, Resources, Supervision, A.W. Goldrath: Conceptualization, Data curation, Formal analysis, Funding acquisition, Investigation, Methodology, Project administration, Resources, Software, Supervision, Validation, Writing - original draft, Writing - review & editing.

Disclosures: A. Ferry reported other from TCura Bioscience outside the submitted work; in addition, A. Ferry had a patent application pending. M. Reina-Campos and A.W. Goldrath are co-founders and scientific advisory board members of TCura Bioscience, Inc. J.S. Gutkind reported non-financial support from Kadima Pharmaceuticals, Inc., and personal fees from Pangea Therapeutics, BTB Therapeutics, Radionetics, I90 LLC, and Domain Pharmaceuticals during the conduct of the study. A.W. Goldrath reported personal fees from ArsenalBio during the conduct of the study and other from ArsenalBio outside the submitted work; in addition, A.W. Goldrath had a patent pending. No other disclosures were reported.

Submitted: 3 May 2024
Revised: 21 October 2024
Accepted: 20 December 2024

References

JungI.Y., E. Noguera-Ortega, R. Bartoszek, S.M. Collins, E. Williams, M. Davis, J.K. Jadlowsky, G. Plesa, D.L. Siegel, A. Chew, et al. 2023. Tissue-resident memory CAR T cells with stem-like characteristics display enhanced efficacy against solid and liquid tumors. *Cell Rep. Med.* 4: 101053. https://doi.org/10.1016/j.xcrm.2023.101053

Banchereau, R., A.S. Chitre, A. Scherl, T.D. Wu, N.S. Patil, P. de Almeida, E.E. Kadel Iii, S. Madireddi, A. Au-Yeung, C. Takahashi, et al. 2021. Intratumoral CD103+ CD8+ T cells predict response to PD-L1 blockade. *J. Immunother. Cancer*. 9:e002231. https://doi.org/10.1136/jitc-2020-002231

Barry, K.C., J. Hsu, M.L. Broz, F.J. Cueto, M. Binnewies, A.J. Combes, A.E. Nelson, K. Loo, R. Kumar, M.D. Rosenblum, et al. 2018. A natural killer-dendritic cell axis defines checkpoint therapy-responsive tumor microenvironments. *Nat. Med.* 24:1178–1191. https://doi.org/10.1038/s41591-018-0085-8

Bayerl, F., P. Meiser, S. Donakonda, A. Hirschberger, S.B. Lacher, A.M. Pedde, C.D. Hermann, A. Elewaut, M. Knolle, L. Ramsauer, et al. 2023. Tumor-derived prostaglandin E2 programs cDC1 dysfunction to impair intratumoral orchestration of anti-cancer T cell responses. *Immunity*. 56: 1341–1358.e11. https://doi.org/10.1016/j.immuni.2023.05.011

Boland, B.S., Z. He, M.S. Tsai, J.G. Olvera, K.D. Omilusik, H.G. Duong, E.S. Kim, A.E. Limary, W. Jin, J.J. Milner, et al. 2020. Heterogeneity and clonal relationships of adaptive immune cells in ulcerative colitis revealed by single-cell analyses. *Sci. Immunol.* 5:eabb4432. https://doi.org/10.1126/sciimmunol.abb4432

Borges da Silva, H., C. Peng, H. Wang, K.M. Wanhainen, C. Ma, S. Lopez, A. Khoruts, N. Zhang, and S.C. Jameson. 2020. Sensing of ATP via the purinergic receptor P2RX7 promotes CD8$^+$ trm cell generation by enhancing their sensitivity to the cytokine TGF-β. *Immunity*. 53: 158–171.e6. https://doi.org/10.1016/j.immuni.2020.06.010

Böttcher, J.P., E. Bonavita, P. Chakravarty, H. Blees, M. Cabeza-Cabrerizo, S. Sammicheli, N.C. Rogers, E. Sahai, S. Zelenay, and C. Reis e Sousa. 2018. NK cells stimulate recruitment of cDC1 into the tumor microenvironment promoting cancer immune control. *Cell*. 172:1022–1037.e14. https://doi.org/10.1016/j.cell.2018.01.004

Bourdely, P., G. Anselmi, K. Vaivode, R.N. Ramos, Y. Missolo-Koussou, S. Hidalgo, J. Tosselo, N. Nuñez, W. Richer, A. Vincent-Salomon, et al. 2020. Transcriptional and functional analysis of CD1c$^+$ human dendritic cells identifies a CD163$^+$ subset priming CD8$^+$CD103$^+$ T cells. *Immunity*. 53:335–352.e8. https://doi.org/10.1016/j.immuni.2020.06.002

Brinkman, E.K., A.N. Kousholt, T. Harmsen, C. Leemans, T. Chen, J. Jonkers, and B. van Steensel. 2018. Easy quantification of template-directed CRISPR/Cas9 editing. *Nucleic Acids Res.* 46:e58. https://doi.org/10.1093/nar/gky164

Chang, J.T., E.J. Wherry, and A.W. Goldrath. 2014. Molecular regulation of effector and memory T cell differentiation. *Nat. Immunol.* 15:1104–1115. https://doi.org/10.1038/ni.3031

Crowl, J.T., M. Heeg, A. Ferry, J.J. Milner, K.D. Omilusik, C. Toma, Z. He, J.T. Chang, and A.W. Goldrath. 2022. Tissue-resident memory CD8$^+$ T cells possess unique transcriptional, epigenetic and functional adaptations to different tissue environments. *Nat. Immunol.* 23:1121–1131. https://doi.org/10.1038/s41590-022-01229-8

Dähling, S., A.M. Mansilla, K. Knöpper, A. Grafen, D.T. Utzschneider, M. Ugur, P.G. Whitney, A. Bachem, P. Arampatzi, F. Imdahl, et al. 2022. Type 1 conventional dendritic cells maintain and guide the differentiation of precursors of exhausted T cells in distinct cellular niches. *Immunity*. 55:656–670.e8. https://doi.org/10.1016/j.immuni.2022.03.006

Domenjo-Vila, E., V. Casella, R. Iwabuchi, E. Fossum, M. Pedragosa, Q. Castellví, P. Cebollada Rica, T. Kaisho, K. Terahara, G. Bocharov, et al. 2023. XCR1+ DCs are critical for T cell-mediated immunotherapy of chronic viral infections. *Cell Rep.* 42:112123. https://doi.org/10.1016/j.celrep.2023.112123

Dorner, B.G., A. Scheffold, M.S. Rolph, M.B. Huser, S.H. Kaufmann, A. Radbruch, I.E. Flesch, and R.A. Kroczek. 2002. MIP-1alpha, MIP-1beta, RANTES, and ATAC/lymphotactin function together with IFN-gamma as type 1 cytokines. *Proc. Natl. Acad. Sci. USA*. 99:6181–6186. https://doi.org/10.1073/pnas.092141999

Dorner, B.G., M.B. Dorner, X. Zhou, C. Opitz, A. Mora, S. Güttler, A. Hutloff, H.W. Mages, K. Ranke, M. Schaefer, et al. 2009. Selective expression of the chemokine receptor XCR1 on cross-presenting dendritic cells

determines cooperation with CD8+ T cells. *Immunity*. 31:823–833. https://doi.org/10.1016/j.immuni.2009.08.027

Edwards, J., J.S. Wilmott, J. Madore, T.N. Gide, C. Quek, A. Tasker, A. Ferguson, J. Chen, R. Hewavisenti, P. Hersey, et al. 2018. CD103$^+$ tumor-resident CD8$^+$ T cells are associated with improved survival in immunotherapy-naïve melanoma patients and expand significantly during anti-PD-1 treatment. *Clin. Cancer Res.* 24:3036–3045. https://doi.org/10.1158/1078-0432.CCR-17-2257

Escobar, G., K. Tooley, J.P. Oliveras, L. Huang, H. Cheng, M.L. Bookstaver, C. Edwards, E. Froimchuk, C. Xue, D. Mangani, et al. 2023. Tumor immunogenicity dictates reliance on TCF1 in CD8+ T cells for response to immunotherapy. *Cancer Cell*. 41:1662–1679.e7. https://doi.org/10.1016/j.ccell.2023.08.001

Frizzell, H., R. Fonseca, S.N. Christo, M. Evrard, S. Cruz-Gomez, N.G. Zanluqui, B. von Scheidt, D. Freestone, S.L. Park, H.E.G. McWilliam, et al. 2020. Organ-specific isoform selection of fatty acid-binding proteins in tissue-resident lymphocytes. *Sci. Immunol.* 5:eaay9283. https://doi.org/10.1126/sciimmunol.aay9283

Ganesan, A.P., J. Clarke, O. Wood, E.M. Garrido-Martin, S.J. Chee, T. Mellows, D. Samaniego-Castruita, D. Singh, G. Seumois, A. Alzetani, et al. 2017. Tissue-resident memory features are linked to the magnitude of cytotoxic T cell responses in human lung cancer. *Nat. Immunol.* 18:940–950. https://doi.org/10.1038/ni.3775

Ghilas, S., M. Ambrosini, J.C. Cancel, C. Brousse, M. Massé, H. Lelouard, M. Dalod, and K. Crozat. 2021. Natural killer cells and dendritic epidermal γδ T cells orchestrate type 1 conventional DC spatiotemporal repositioning toward CD8$^+$ T cells. *iScience*. 24:103059. https://doi.org/10.1016/j.isci.2021.103059

Giles, J.R., A.M. Globig, S.M. Kaech, and E.J. Wherry. 2023. CD8$^+$ T cells in the cancer-immunity cycle. *Immunity*. 56:2231–2253. https://doi.org/10.1016/j.immuni.2023.09.005

Heiss, K., N. Jänner, B. Mähnss, V. Schumacher, F. Koch-Nolte, F. Haag, and H.-W. Mittrücker. 2008. High sensitivity of intestinal CD8+ T cells to nucleotides indicates P2X7 as a regulator for intestinal T cell responses. *J. Immunol.* 181:3861–3869. https://doi.org/10.4049/jimmunol.181.6.3861

Hildner, K., B.T. Edelson, W.E. Purtha, M. Diamond, H. Matsushita, M. Kohyama, B. Calderon, B.U. Schraml, E.R. Unanue, M.S. Diamond, et al. 2008. Batf3 deficiency reveals a critical role for CD8α+ dendritic cells in cytotoxic T cell immunity. *Science*. 322:1097–1100. https://doi.org/10.1126/science.1164206

Hombrink, P., C. Helbig, R.A. Backer, B. Piet, A.E. Oja, R. Stark, G. Brasser, A. Jongejan, R.E. Jonkers, B. Nota, et al. 2016. Programs for the persistence, vigilance and control of human CD8$^+$ lung-resident memory T cells. *Nat. Immunol.* 17:1467–1478. https://doi.org/10.1038/ni.3589

Hudson, W.H., J. Gensheimer, M. Hashimoto, A. Wieland, R.M. Valanparambil, P. Li, J.X. Lin, B.T. Konieczny, S.J. Im, G.J. Freeman, et al. 2019. Proliferating transitory T cells with an effector-like transcriptional signature emerge from PD-1$^+$ stem-like CD8$^+$ T cells during chronic infection. *Immunity*. 51:1043–1058.e4. https://doi.org/10.1016/j.immuni.2019.11.002

Iborra, S., M. Martínez-López, S.C. Khouili, M. Enamorado, F.J. Cueto, R. Conde-Garrosa, C. Del Fresno, and D. Sancho. 2016. Optimal generation of tissue-resident but not circulating memory T cells during viral infection requires crosspriming by DNGR-1$^+$ dendritic cells. *Immunity*. 45:847–860. https://doi.org/10.1016/j.immuni.2016.08.019

Im, S.J., M. Hashimoto, M.Y. Gerner, J. Lee, H.T. Kissick, M.C. Burger, Q. Shan, J.S. Hale, J. Lee, T.H. Nasti, et al. 2016. Defining CD8+ T cells that provide the proliferative burst after PD-1 therapy. *Nature*. 537:417–421. https://doi.org/10.1038/nature19330

Iwata, M., A. Hirakiyama, Y. Eshima, H. Kagechika, C. Kato, and S.Y. Song. 2004. Retinoic acid imprints gut-homing specificity on T cells. *Immunity*. 21:527–538. https://doi.org/10.1016/j.immuni.2004.08.011

Jadhav, R.R., S.J. Im, B. Hu, M. Hashimoto, P. Li, J.X. Lin, W.J. Leonard, W.J. Greenleaf, R. Ahmed, and J.J. Goronzy. 2019. Epigenetic signature of PD-1+ TCF1+ CD8 T cells that act as resource cells during chronic viral infection and respond to PD-1 blockade. *Proc. Natl. Acad. Sci. USA*. 116:14113–14118. https://doi.org/10.1073/pnas.1903520116

Jansen, C.S., N. Prokhnevska, V.A. Master, M.G. Sanda, J.W. Carlisle, M.A. Bilen, M. Cardenas, S. Wilkinson, R. Lake, A.G. Sowalsky, et al. 2019. An intra-tumoral niche maintains and differentiates stem-like CD8 T cells. *Nature*. 576:465–470. https://doi.org/10.1038/s41586-019-1836-5

Kumar, B.V., W. Ma, M. Miron, T. Granot, R.S. Guyer, D.J. Carpenter, T. Senda, X. Sun, S.H. Ho, H. Lerner, et al. 2017. Human tissue-resident memory T cells are defined by core transcriptional and functional signatures in lymphoid and mucosal sites. *Cell Rep.* 20:2921–2934. https://doi.org/10.1016/j.celrep.2017.08.078

Kurd, N.S., Z. He, T.L. Louis, J.J. Milner, K.D. Omilusik, W. Jin, M.S. Tsai, C.E. Widjaja, J.N. Kanbar, J.G. Olvera, et al. 2020. Early precursors and molecular determinants of tissue-resident memory CD8$^+$ T lymphocytes revealed by single-cell RNA sequencing. *Sci. Immunol.* 5:eaaz6894. https://doi.org/10.1126/sciimmunol.aaz6894

Lei, Y., A.M. Ripen, N. Ishimaru, I. Ohigashi, T. Nagasawa, L.T. Jeker, M.R. Bösl, G.A. Holländer, Y. Hayashi, R.W. Malefyt, et al. 2011. Aire-dependent production of XCL1 mediates medullary accumulation of thymic dendritic cells and contributes to regulatory T cell development. *J. Exp. Med.* 208:383–394. https://doi.org/10.1084/jem.20102327

Lei, Y., and Y. Takahama. 2012. XCL1 and XCR1 in the immune system. *Microbes Infect.* 14:262–267. https://doi.org/10.1016/j.micinf.2011.10.003

van der Leun, A.M., D.S. Thommen, and T.N. Schumacher. 2020. CD8$^+$ T cell states in human cancer: Insights from single-cell analysis. *Nat. Rev. Cancer*. 20:218–232. https://doi.org/10.1038/s41568-019-0235-4

Luda, K.M., T. Joeris, E.K. Persson, A. Rivollier, M. Demiri, K.M. Sitnik, L. Pool, J.B. Holm, F. Melo-Gonzalez, L. Richter, et al. 2016. IRF8 transcription-factor-dependent classical dendritic cells are essential for intestinal T cell homeostasis. *Immunity*. 44:860–874. https://doi.org/10.1016/j.immuni.2016.02.008

Mani, V., S.K. Bromley, T. Äijö, R. Mora-Buch, E. Carrizosa, R.D. Warner, M. Hamze, D.R. Sen, A.Y. Chasse, A. Lorant, et al. 2019. Migratory DCs activate TGF-β to precondition naïve CD8$^+$ T cells for tissue-resident memory fate. *Science*. 366:eaav5728. https://doi.org/10.1126/science.aav5728

Meiser, P., M.A. Knolle, A. Hirschberger, G.P. de Almeida, F. Bayerl, S. Lacher, A.M. Pedde, S. Flommersfeld, J. Hönninger, L. Stark, et al. 2023. A distinct stimulatory cDC1 subpopulation amplifies CD8$^+$ T cell responses in tumors for protective anti-cancer immunity. *Cancer Cell*. 41:1498–1515.e10. https://doi.org/10.1016/j.ccell.2023.06.008

Mempel, T.R., S.E. Henrickson, and U.H. Von Andrian. 2004. T-cell priming by dendritic cells in lymph nodes occurs in three distinct phases. *Nature*. 427:154–159. https://doi.org/10.1038/nature02238

Miller, B.C., D.R. Sen, R. Al Abosy, K. Bi, Y.V. Virkud, M.W. LaFleur, K.B. Yates, A. Lako, K. Felt, G.S. Naik, et al. 2019. Subsets of exhausted CD8$^+$ T cells differentially mediate tumor control and respond to checkpoint blockade. *Nat. Immunol.* 20:326–336. https://doi.org/10.1038/s41590-019-0312-6

Milner, J.J., and A.W. Goldrath. 2018. Transcriptional programming of tissue-resident memory CD8$^+$ T cells. *Curr. Opin. Immunol.* 51:162–169. https://doi.org/10.1016/j.coi.2018.03.017

Milner, J.J., C. Toma, Z. He, N.S. Kurd, Q.P. Nguyen, B. McDonald, L. Quezada, C.E. Widjaja, D.A. Witherden, J.T. Crowl, et al. 2020. Heterogenous populations of tissue-resident CD8$^+$ T cells are generated in response to infection and malignancy. *Immunity*. 52:808–824.e7. https://doi.org/10.1016/j.immuni.2020.04.007

Milner, J.J., C. Toma, B. Yu, K. Zhang, K. Omilusik, A.T. Phan, D. Wang, A.J. Getzler, T. Nguyen, S. Crotty, et al. 2017. Runx3 programs CD8$^+$ T cell residency in non-lymphoid tissues and tumours. *Nature*. 552:253–257. https://doi.org/10.1038/nature24993

Molenaar, R., M. Knippenberg, G. Goverse, B.J. Olivier, A.F. de Vos, T. O'Toole, and R.E. Mebius. 2011. Expression of retinaldehyde dehydrogenase enzymes in mucosal dendritic cells and gut-draining lymph node stromal cells is controlled by dietary vitamin A. *J. Immunol.* 186:1934–1942. https://doi.org/10.4049/jimmunol.1001672

Mora, J.R., M.R. Bono, N. Manjunath, W. Weninger, L.L. Cavanagh, M. Rosemblatt, and U.H. Von Andrian. 2003. Selective imprinting of gut-homing T cells by Peyer's patch dendritic cells. *Nature*. 424:88–93. https://doi.org/10.1038/nature01726

Nakandakari-Higa, S., S. Walker, M.C.C. Canesso, V. van der Heide, A. Chudnovskiy, D.-Y. Kim, J.T. Jacobsen, R. Parsa, J. Bilanovic, S.M. Parigi, et al. 2024. Universal recording of immune cell interactions in vivo. *Nature*. 627:399–406. https://doi.org/10.1038/s41586-024-07134-4

Nath, A.P., A. Braun, S.C. Ritchie, F.R. Carbone, L.K. Mackay, T. Gebhardt, and M. Inouye. 2019. Comparative analysis reveals a role for TGF-β in shaping the residency-related transcriptional signature in tissue-resident memory CD8+ T cells. *PLoS One*. 14:e0210495. https://doi.org/10.1371/journal.pone.0210495

Nüssing, S., I.G. House, C.J. Kearney, A.X.Y. Chen, S.J. Vervoort, P.A. Beavis, J. Oliaro, R.W. Johnstone, J.A. Trapani, and I.A. Parish. 2020. Efficient CRISPR/Cas9 gene editing in uncultured naive mouse T cells for in vivo studies. *J. Immunol.* 204:2308–2315. https://doi.org/10.4049/jimmunol.1901396

Ohta, T., M. Sugiyama, H. Hemmi, C. Yamazaki, S. Okura, I. Sasaki, Y. Fukuda, T. Orimo, K.J. Ishii, K. Hoshino, et al. 2016. Crucial roles of XCR1-expressing dendritic cells and the XCR1-XCL1 chemokine axis in

intestinal immune homeostasis. *Sci. Rep.* 6:23505. https://doi.org/10.1038/srep23505

Okła, K., D.L. Farber, and W. Zou. 2021. Tissue-resident memory T cells in tumor immunity and immunotherapy. *J. Exp. Med.* 218:e20201605. https://doi.org/10.1084/jem.20201605

Oliveira, G., A.M. Egloff, A.B. Afeyan, J.O. Wolff, Z. Zeng, R.D. Chernock, L. Zhou, C. Messier, P. Lizotte, K.L. Pfaff, et al. 2023. Preexisting tumor-resident T cells with cytotoxic potential associate with response to neoadjuvant anti–PD-1 in head and neck cancer. *Sci. Immunol.* 8: eadf4968. https://doi.org/10.1126/sciimmunol.adf4968

Ozga, A.J., M.T. Chow, and A.D. Luster. 2021. Chemokines and the immune response to cancer. *Immunity*. 54:859–874. https://doi.org/10.1016/j.immuni.2021.01.012

Park, S.L., A. Buzzai, J. Rautela, J.L. Hor, K. Hochheiser, M. Effern, N. McBain, T. Wagner, J. Edwards, R. McConville, et al. 2019. Tissue-resident memory CD8$^+$ T cells promote melanoma-immune equilibrium in skin. *Nature*. 565:366–371. https://doi.org/10.1038/s41586-018-0812-9

Peperzak, V., E.A.M. Veraar, Y. Xiao, N. Bąbała, K. Thiadens, M. Brugmans, and J. Borst. 2013. CD8+ T cells produce the chemokine CXCL10 in response to CD27/CD70 costimulation to promote generation of the CD8+ effector T cell pool. *J. Immunol.* 191:3025–3036. https://doi.org/10.4049/jimmunol.1202222

Di Pilato, M., R. Kfuri-Rubens, J.N. Pruessmann, A.J. Ozga, M. Messemaker, B.L. Cadilha, R. Sivakumar, C. Cianciaruso, R.D. Warner, F. Marangoni, et al. 2021. CXCR6 positions cytotoxic T cells to receive critical survival signals in the tumor microenvironment. *Cell*. 184:4512–4530.e22. https://doi.org/10.1016/j.cell.2021.07.015

Qiu, Z., C. Khairallah, T.H. Chu, J.N. Imperato, X. Lei, G. Romanov, A. Atakilit, L. Puddington, and B.S. Sheridan. 2023. Retinoic acid signaling during priming licenses intestinal CD103+ CD8 TRM cell differentiation. *J. Exp. Med.* 220:e20210923. https://doi.org/10.1084/jem.20210923

Reina-Campos, M., M. Heeg, K. Kennewick, I.T. Mathews, G. Galletti, V. Luna, Q. Nguyen, H. Huang, J.J. Milner, K.H. Hu, et al. 2023. Metabolic programs of T cell tissue residency empower tumour immunity. *Nature*. 621:179–187. https://doi.org/10.1038/s41586-023-06483-w

Reina-Campos, M., A. Monell, A. Ferry, V. Luna, K.P. Cheung, G. Galletti, N.E. Scharping, K.K. Takehara, S. Quon, B. Boland, et al. 2024. Functional diversity of memory CD8 T cells is spatiotemporally imprinted. *bioRxiv*. https://doi.org/10.1101/2024.03.20.585130 (Preprint posted March 25, 2024).

Russ, B.E., M. Olshanksy, H.S. Smallwood, J. Li, A.E. Denton, J.E. Prier, A.T. Stock, H.A. Croom, J.G. Cullen, M.L. Nguyen, et al. 2014. Distinct epigenetic signatures delineate transcriptional programs during virus-specific CD8(+) T cell differentiation. *Immunity*. 41:853–865. https://doi.org/10.1016/j.immuni.2014.11.001

Sade-Feldman, M., K. Yizhak, S.L. Bjorgaard, J.P. Ray, C.G. de Boer, R.W. Jenkins, D.J. Lieb, J.H. Chen, D.T. Frederick, M. Barzily-Rokni, et al. 2018. Defining T cell states associated with response to checkpoint immunotherapy in melanoma. *Cell*. 175:998–1013.e20. https://doi.org/10.1016/j.cell.2018.10.038

Salmon, H., J. Idoyaga, A. Rahman, M. Leboeuf, R. Remark, S. Jordan, M. Casanova-Acebes, M. Khudoynazarova, J. Agudo, N. Tung, et al. 2016. Expansion and activation of CD103(+) dendritic cell progenitors at the tumor site enhances tumor responses to therapeutic PD-L1 and BRAF inhibition. *Immunity*. 44:924–938. https://doi.org/10.1016/j.immuni.2016.03.012

Sautès-Fridman, C., F. Petitprez, J. Calderaro, and W.H. Fridman. 2019. Tertiary lymphoid structures in the era of cancer immunotherapy. *Nat. Rev. Cancer*. 19:307–325. https://doi.org/10.1038/s41568-019-0144-6

Savas, P., B. Virassamy, C. Ye, A. Salim, C.P. Mintoff, F. Caramia, R. Salgado, D.J. Byrne, Z.L. Teo, S. Dushyanthen, et al. 2018. Single-cell profiling of breast cancer T cells reveals a tissue-resident memory subset associated with improved prognosis. *Nat. Med.* 24:986–993. https://doi.org/10.1038/s41591-018-0078-7

Schenkel, J.M., K.A. Fraser, L.K. Beura, K.E. Pauken, V. Vezys, and D. Masopust. 2014. T cell memory. Resident memory CD8 T cells trigger protective innate and adaptive immune responses. *Science*. 346:98–101. https://doi.org/10.1126/science.1254536

Schenkel, J.M., and K.E. Pauken. 2023. Localization, tissue biology and T cell state - implications for cancer immunotherapy. *Nat. Rev. Immunol.* 23: 807–823. https://doi.org/10.1038/s41577-023-00884-8

Shiokawa, A., R. Kotaki, T. Takano, H. Nakajima-Adachi, and S. Hachimura. 2017. Mesenteric lymph node CD11b$^-$ CD103$^+$ PD-L1^{High} dendritic cells highly induce regulatory T cells. *Immunology*. 152:52–64. https://doi.org/10.1111/imm.12747

Siddiqui, I., K. Schaeuble, V. Chennupati, S.A. Fuertes Marraco, S. Calderon-Copete, D. Pais Ferreira, S.J. Carmona, L. Scarpellino, D. Gfeller, S. Pradervand, et al. 2019. Intratumoral Tcf1$^+$PD-1$^+$CD8$^+$ T cells with stem-like properties promote tumor control in response to vaccination and checkpoint blockade immunotherapy. *Immunity*. 50:195–211.e10. https://doi.org/10.1016/j.immuni.2018.12.021

Spranger, S., D. Dai, B. Horton, and T.F. Gajewski. 2017. Tumor-residing Batf3 dendritic cells are required for effector T cell trafficking and adoptive T cell therapy. *Cancer Cell*. 31:711–723.e4. https://doi.org/10.1016/j.ccell.2017.04.003

Steinert, E.M., J.M. Schenkel, K.A. Fraser, L.K. Beura, L.S. Manlove, B.Z. Igyártó, P.J. Southern, and D. Masopust. 2015. Quantifying memory CD8 T cells reveals regionalization of immunosurveillance. *Cell*. 161:737–749. https://doi.org/10.1016/j.cell.2015.03.031

Stoltzfus, C.R., R. Sivakumar, L. Kunz, B.E. Olin Pope, E. Menietti, D. Speziale, R. Adelfio, M. Bacac, S. Colombetti, M. Perro, and M.Y. Gerner. 2021. Multi-parameter quantitative imaging of tumor microenvironments reveals perivascular immune niches associated with anti-tumor immunity. *Front. Immunol.* 12:726492. https://doi.org/10.3389/fimmu.2021.726492

Tang, Z., B. Kang, C. Li, T. Chen, and Z. Zhang. 2019. GEPIA2: An enhanced web server for large-scale expression profiling and interactive analysis. *Nucleic Acids Res.* 47:W556–W560. https://doi.org/10.1093/nar/gkz430

Teijeira, A., S. Garasa, C. Luri-Rey, C. de Andrea, M. Gato, C. Molina, T. Kaisho, A. Cirella, A. Azpilikueta, S.K. Wculek, et al. 2022. Depletion of conventional type-1 dendritic cells in established tumors suppresses immunotherapy efficacy. *Cancer Res.* 82:4373–4385. https://doi.org/10.1158/0008-5472.CAN-22-1046

Wang, X.Q., E. Danenberg, C.-S. Huang, D. Egle, M. Callari, B. Bermejo, M. Dugo, C. Zamagni, M. Thill, A. Anton, et al. 2023. Spatial predictors of immunotherapy response in triple-negative breast cancer. *Nature*. 621: 868–876. https://doi.org/10.1038/s41586-023-06498-3

Wculek, S.K., F.J. Cueto, A.M. Mujal, I. Melero, M.F. Krummel, and D. Sancho. 2020. Dendritic cells in cancer immunology and immunotherapy. *Nat. Rev. Immunol.* 20:7–24. https://doi.org/10.1038/s41577-019-0210-z

Wherry, E.J., J.N. Blattman, K. Murali-Krishna, R. van der Most, and R. Ahmed. 2003. Viral persistence alters CD8 T-cell immunodominance and tissue distribution and results in distinct stages of functional impairment. *J. Virol.* 77:4911–4927. https://doi.org/10.1128/jvi.77.8.4911-4927.2003

Yamazaki, C., M. Sugiyama, T. Ohta, H. Hemmi, E. Hamada, I. Sasaki, Y. Fukuda, T. Yano, M. Nobuoka, T. Hirashima, et al. 2013. Critical roles of a dendritic cell subset expressing a chemokine receptor, XCR1. *J. Immunol.* 190:6071–6082. https://doi.org/10.4049/jimmunol.1202798

Zhang, N., and M.J. Bevan. 2013. Transforming growth factor-β signaling controls the formation and maintenance of gut-resident memory T cells by regulating migration and retention. *Immunity*. 39:687–696. https://doi.org/10.1016/j.immuni.2013.08.019

Zheng, L., S. Qin, W. Si, A. Wang, B. Xing, R. Gao, X. Ren, L. Wang, X. Wu, J. Zhang, et al. 2021. Pan-cancer single-cell landscape of tumor-infiltrating T cells. *Science*. 374:abe6474. https://doi.org/10.1126/science.abe6474

Supplemental material

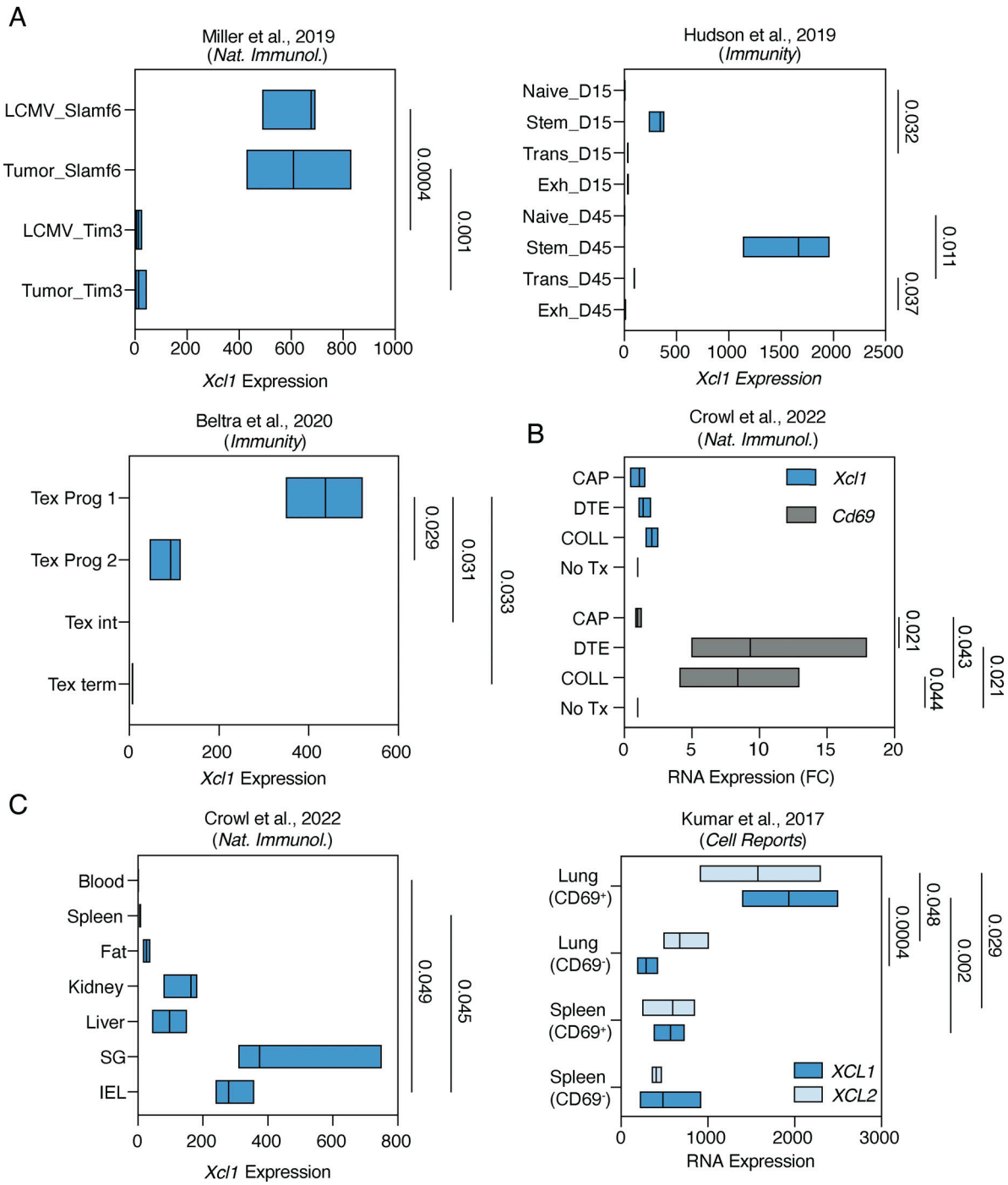

Figure S1. **Expression of *Xcl1* and *XCL2* (human) across CD8⁺ T cell subsets. (A)** *Xcl1* gene expression in P14 T cells derived from indicated studies. Top left: Expression data during LCMV-Cl13 chronic viral infection and B16 melanoma challenge in indicated subsets. Top right: Expression data during LCMV-Cl13 in indicated subsets and time points. Bottom left: Expression data during LCMV-Cl13 using alternative gating scheme. **(B)** Splenic CD8⁺ T cell gene expression of *Xcl1* and *CD69* using different tissue digestion methods. **(C)** Expression data from CD8⁺ T_{RM} during LCMV-Arm (left) and *XCL1* and *XCL2* gene expression in human CD8⁺ T cells in indicated subsets (right). P values shown. Two-way ANOVA (A–C).

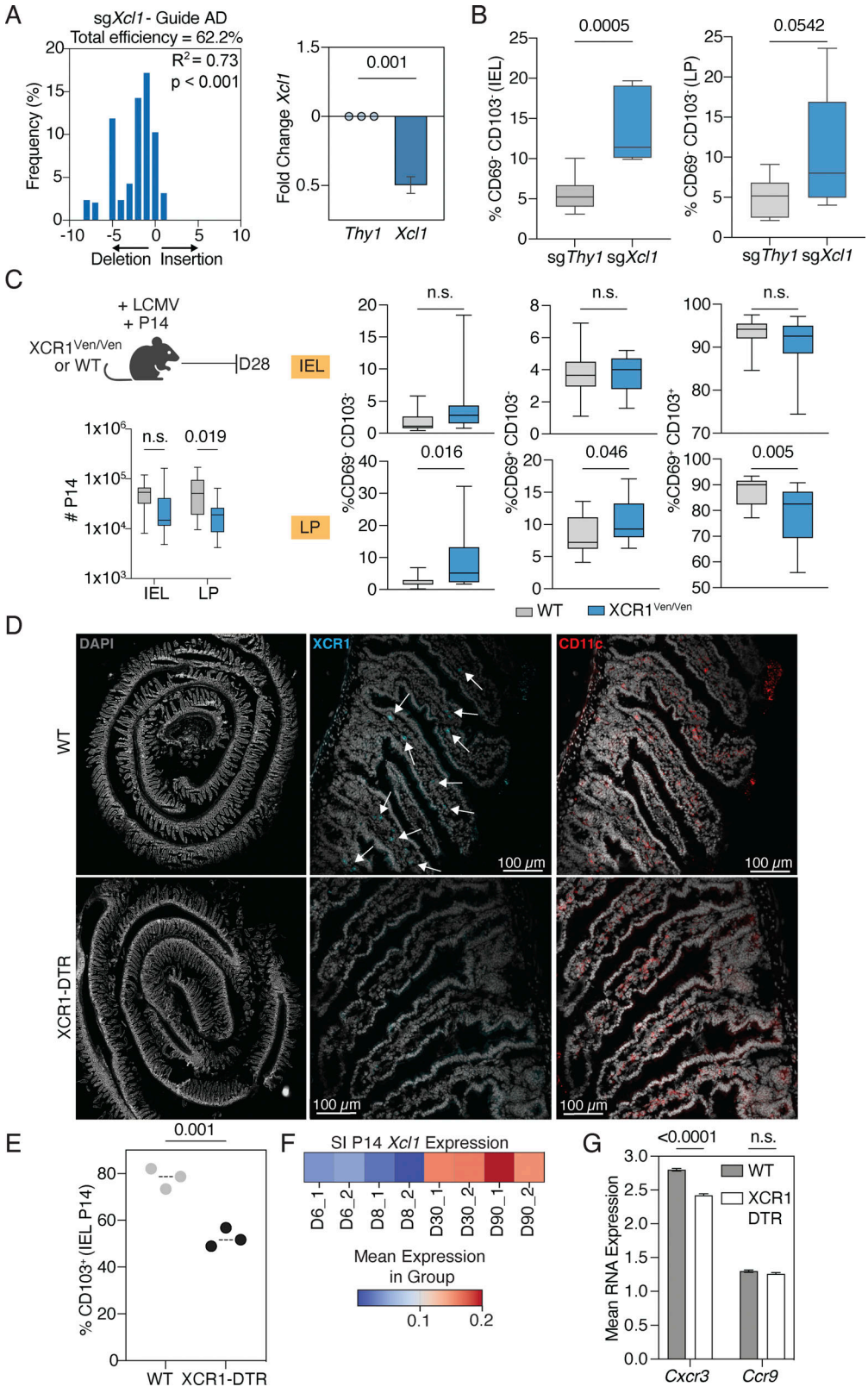

Figure S2. **Confirmation of XCR1⁺ depletion and whole tissue microscopy. (A)** CRISPR targeting efficiency (TIDE) and *Xcl1* qPCR data. **(B)** Quantification of CD69⁻ CD103⁻ population in IEL and LP D25 following LCMV-Arm. **(C)** Experiment setup in which naïve P14 T cells transferred into WT or XCR1$^{Ven/Ven}$ (left). Subset frequencies of IEL and LP P14 T cells and cell numbers. **(D)** Confocal imaging validation of XCR1⁺ cell depletion in SI following DT treatment. Marker colors indicated in panel. **(E)** Quantification of IEL CD103⁺ P14 T cell frequency at D8, each dot represents one mouse. **(F)** *Xcl1* gene expression in SI P14 T cells during LCMV-Arm timecourse. **(G)** Spatial transcriptomic mean RNA expression of *Cxcr3* and *Ccr9* P14 T cells. P value shown, unpaired *t* test (A–C and E) and two-way ANOVA (C and G).

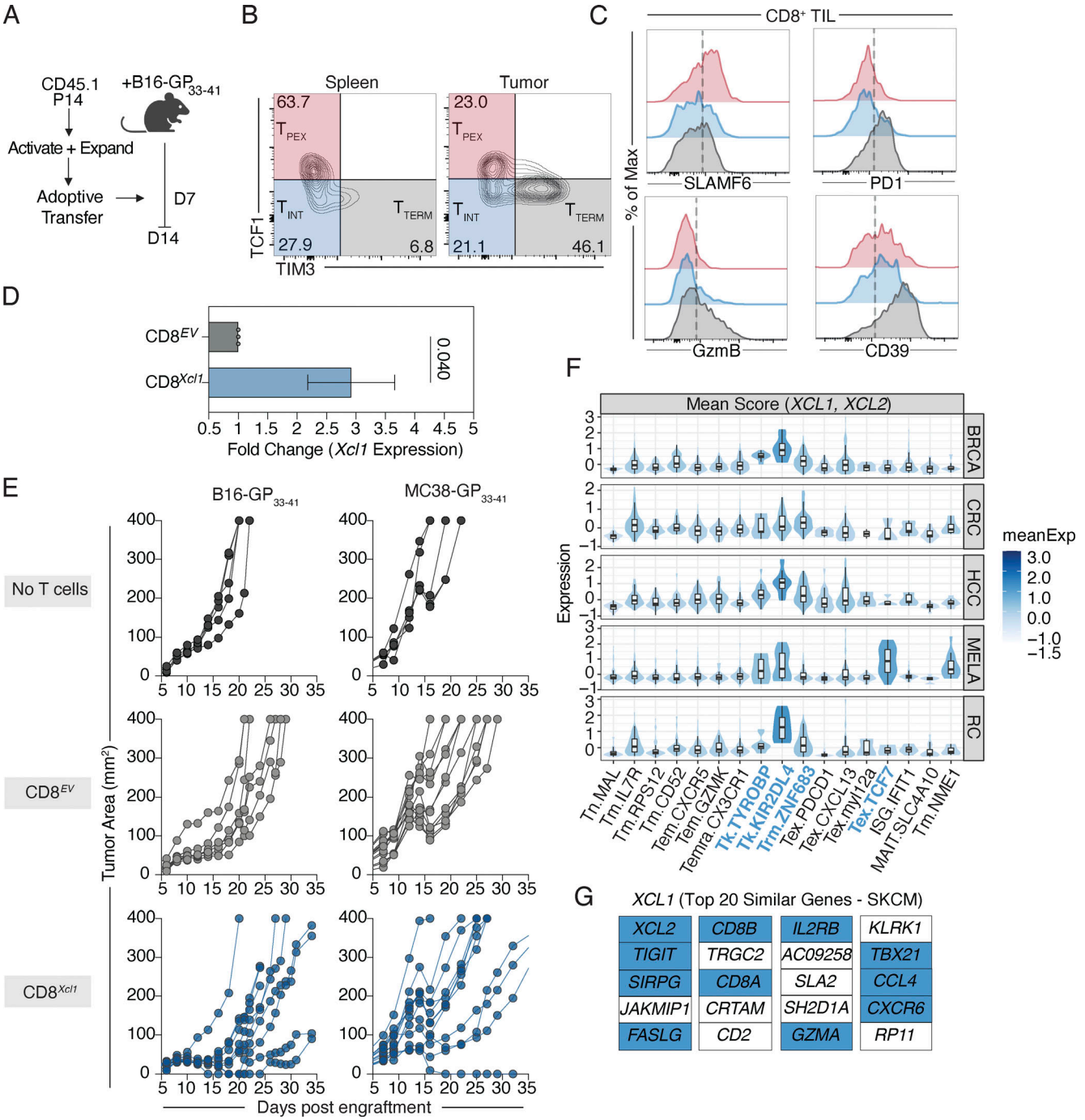

Figure S3. **Murine CD8⁺ TIL phenotyping and human XCL1/XCL2 expression profile. (A)** Experiment setup in which preactivated P14 T cells were transferred into tumor-bearing mice, followed by tissue analysis D7 after transfer. **(B)** Representative plots of P14 in indicated tissue, subset label shown, $n = 5$. **(C)** Representative histograms of marker expression within the indicated subset defined by TCF1 and TIM3. **(D)** qPCR validation of *Xcl1* overexpression in P14 T cells. **(E)** Tumor growth curves of mice receiving no T cells, $CD8^{EV}$, and $CD8^{Xcl1}$. Each line represents an individual mouse. **(F)** Mean expression of *XCL1* and *XCL2* across annotated clusters within five human tumor types. Clusters with high expression (Fig. 4 F) are highlighted in blue. **(G)** Top 20 genes with similar expression profile to *XCL1* in SKCM. Genes of interest are highlighted in blue (GEPIA 2.0). Data representative of at least two independent experiments (B–E). P value shown, unpaired *t* test (D).